UNIVERSITY OF TWENTE.

Bachelor of Applied Physics

Engineering Fluid Dynamics
CTW-EFD
Bachelor thesis

Flow field visualization and input waveform optimization for a linear plasma synthetic jet actuator

S.H. Sterl
C.E. van Ommeren

August 2012

TS-137

UNIVERSITY OF TWENTE.

Bachelor Thesis

Flow field visualization and input waveform optimization for a linear plasma synthetic jet actuator

---

Authors:
Christiaan van Ommeren
Sebastian Sterl

Supervisors:
Prof. dr. ir. H.W.M. Hoeijmakers
Dr. C. Sun

August 23, 2012

Abstract

The performance of a linear plasma synthetic jet actuator (L-PSJA) has been experimentally investigated as a function of the input wave train pulsing frequency and duty cycle. Visualization of the induced velocity profiles has been performed using Particle Image Velocimetry.

The used PSJA design consisted of two horizontally separated, exposed copper electrodes mounted on a plate of Duran glass of 2 mm thickness, with a third, grounded electrode on the other side of this plate. The horizontal gap distance between either of the exposed electrodes and the lower electrode was zero. The input wave train amplitudes were in the range of kilovolts.

Analysis of the velocity profiles reveals that the actuator behaviour shows no dependence on pulsing frequencies in the range 30 Hz to 70 Hz. Furthermore, a significant change in actuator behaviour as a function of duty cycles in the range 20% to 65% has not been observed. The latter indicates an opportunity for reducing energy costs in future industrial applications of PSJA devices.

Maximum values of vertical velocities in the jet, and vertical velocity flux above the actuator, were in almost all cases recorded at distances between 50 mm and 90 mm above the actuator surface. All measured maximum velocities were in the range 0.11 ms^{-1} to 0.25 ms^{-1}. All maximum values of the vertical velocity flux were in the range 0.003 $\mathrm{m}^3\mathrm{s}^{-1}$ to 0.007 $\mathrm{m}^3\mathrm{s}^{-1}$ per meter span. A numerical simulation of PSJA behaviour has been performed, which is able to replicate the order-of-magnitude of the experimentally found velocities, but not the structure of the jets.

The durability of actuators has been found to be a critical point. The used actuator design, when supplied with high-voltage waveforms, lasted only for a short period before damage to the upper electrodes set in. All measurements were therefore performed by replacing the upper electrodes prior to each test. If PSJA devices are to be used in industrial applications, this point must be addressed thoroughly.

Contents

Symbol	Meaning
Physical constants	
ϵ_0	vacuum permittivity ($8.85 \cdot 10^{-12}$ Fm^{-1})
k_B	Boltzmann constant ($1.38 \cdot 10^{-23}$ JK^{-1})
e	unit of charge ($1.60 \cdot 10^{-19}$ C)
Geometry	
x	horizontal coordinate (m)
y	vertical coordinate (m)
Electrostatics	
$\mathbf{E}$	electric field (Vm^{-1})
$\mathbf{D}$	electric displacement field (Cm^{-2})
ϵ_r	dielectric constant
ϵ	dielectric permittivity ($= \epsilon_0 \epsilon_r$) (Fm^{-1})
λ_D	Debye length (m)
Φ	total potential (V)
ϕ_{ext}	externally applied potential (V)
ϕ_{int}	potential due to internal charge buildup (V)
ρ_c	net charge density (Cm^{-3})
$\rho_{c,ext}$	charge density due to ϕ_{ext} (Cm^{-3})
$\rho_{c,int}$	charge density due to ϕ_{int} (Cm^{-3})
n_0	background plasma density (m^{-3})
$n_{i,e}$	density of ions, electrons (m^{-3})
$T_{i,e}$	temperature of ions, electrons (K)
P	power (W)
Fluid dynamics	
Sr	Strouhal number, $\sim$ [frequency] $\cdot$ [length] / [velocity]
U_∞	freestream velocity (ms^{-1})
c_ℓ	lift coefficient
α	angle of attack
$\mathbf{f}$	volume force density (Nm^{-3})
$\mathbf{u}$	flow velocity vector (ms^{-1})
ρ	fluid density (kg$\cdot$m^{-3})
p	pressure (Pa)
μ	dynamic viscosity (kg$\cdot$m^{-1}s^{-1})
$u(x,y,t)$	horizontal velocity component (ms^{-1})
$v(x,y,t)$	vertical velocity component (ms^{-1})
$\overline{v_{max}}$	average of maximum vertical velocities (ms^{-1})
$\overline{v}(x,y)$	time-averaged vertical velocity (ms^{-1})
$\overline{v}_{max}(y)$	maximum along x-axis of $\overline{v}(x,y)$ (ms^{-1})
$Q(y)$	2-dimensional vertical velocity flux, $\int_{jet} \overline{v}(x,y)dx$ (m^{2}s^{-1})
LABview parameters	
A	square wave offset for active duty phase (V)
B	square wave amplitude for active duty phase (V)
C	voltage value for passive duty phase (V)
f_{drive}	driving frequency (Hz)
f_{pulse}	pulse train frequency (Hz)
d	duty cycle fraction ($0 < d < 1$)

Acknowledgements

The authors wish to express their gratitude to the following persons:

Reinder Heukers, as day-to-day supervisor;
ing. Paul Niël and Herman Stobbe, for helping to design and build the experimental setup;
Prof. dr. Harry Hoeijmakers, as main supervisor from the Engineering Fluid Dynamics group;
Dr. Chao Sun, as supervisor from the Physics of Fluids group;
Dr. Yoshiyuki Tagawa, for providing access to the PIV setup;
Dr. Bert Bastiaens, for sharing his knowledge on the theory of plasma actuators;
and the people at the TCO Glass workshop for helping in the construction of the actuators.

Chapter 1

Introduction

Flow control has long been a focus of interest for scientists and engineers. The ability to manipulate flow patterns and control parameters such as lift and drag coefficients is of great importance in the fields of fluid dynamics and aerodynamics. For example, there exists a large need to increase the maximum lift and the lift-to-drag ratio of airfoils, so that airplanes may have lower stalling speeds and experience less resistance during flight. For wind turbines, controlling the flow is useful to ensure a predictable power output and a constant blade load even in fluctuating wind conditions.

Flow control can be either passive or active. Turbulators, vortex generators, or specific geometric shapes, like mechanical flaps and slats, are known as passive flow control techniques, because no external energy is added into the flow. Active devices use external energy to add momentum into the flow.

A recent method of active flow control, based on electrohydrodynamical principles, is called plasma actuation. It is based on injecting momentum into a flow through an electric discharge. By applying high voltage waveforms between two electrodes, an ionic wind can be induced which can be used for flow control purposes such as separation control and load control. It is no surprise that plasma actuators have received much attention over the past decade, since an electrically-operated device could have great advantages over mechanically-operated actuators.

Plasma actuators exist in various designs and types, depending on the application. The simplest design consists of two horizontally separated electrodes, one exposed to the air and one embedded in the material of the object in question, vertically separated by a dielectric layer. Applying a high-frequency, high-voltage waveform between the electrodes can induce a discharge, in which electrons and ionized particles undergo a motion towards one of the electrodes, subject to the influence of the electric field. Through a mechanism that is not yet fully understood, this induced flow injects momentum into the surrounding fluid, creating a wall jet which can delay boundary layer separation, an important aspect in lift and drag control.

Different electrode configurations can be used to create other types of jets. For example, by inducing two wall jets headed towards each other, a vertical jet may be generated. This is called plasma synthetic jet actuation, and is the main subject of this report.

Much research has gone into the performance and optimization of plasma actuators. Both the influence on actuator performance of input parameters, such as waveform, frequency and voltage, and design parameters, such as electrode width and dielectric material type, have been the subject of a number of studies. Furthermore, much attention has gone into visualizing flow patterns and velocity distributions induced by plasma actuation, both in quiescent air and in crossflow.

This report focuses on the characteristics of synthetic jets created by a linear plasma synthetic jet actuator (L-PSJA), as well as on the optimization of the waveform parameters used to operate the actuator. Experiments have been conducted to visualize the jets using Particle Image Velocimetry, at different pulsing frequencies and duty cycles of the input waveform.

Chapter 2 provides background theory on the physics of plasma actuation, research into optimization of plasma actuator design, and the principle of plasma synthetic jet generation. In chapter 3, the experimental setup used in this study is described in detail. Chapter 4 provides an overview and a discussion of the obtained results. In chapter 5, the results of a numerical simulation of this study's L-PSJA can be found, as well as a comparison of numerical and experimental results. Conclusions to the report can be found in chapter 6.

Chapter 2

Principles of plasma actuation

This chapter gives an overview of the theory needed to understand the functioning of plasma actuators, and provides background on research into plasma actuation. First, the principle of gas discharge and the specific type of discharge in plasma actuators is explained; then, some important results regarding the characteristics and optimization of two important kinds of plasma actuators are given - the single dielectric barrier discharge (SDBD) and the plasma synthetic jet actuator (PSJA). Lastly, a brief overview of some notable results in numerical simulations of plasma actuation is given.

2.1 Cold plasmas

A gas is a state of matter in which a substance has neither a definite volume nor a definite shape. The particles that make up a gas have different velocities. The average velocity of these particles can be predicted using the kinetic theory of gases: in the 19th century, James Clerk Maxwell and Ludwig Boltzmann concluded that temperature is a measure of the average kinetic energy of the particles. If a gas is in a state of high temperature, the average kinetic energy of the particles is high, and ionization may occur: a particle can split into an ion and free electrons.

The state of matter in which electrons and ions are separated from each other is called plasma. Plasmas can be categorized as either thermal (also known as 'hot'), or non-thermal ('cold') [1]. If particles ionize due to high temperatures, the plasma is called thermal. For example, if air is considered at an atmospheric pressure and ambient temperature, its chemical composition is approximately 20 percent O_2 and 80 percent N_2, by volume. If the temperature increases, O_2 will start to dissociate first, and at higher temperatures, N_2 will follow. When most of the molecules are dissociated, the ionization of both N and O atoms will take place at around 9000 K [2].

A non-thermal plasma, however, is not induced by a very high temperature, but instead by a potential difference across a gas. One of the first measurements of the current-voltage characteristics of a gas between two electrodes, operated by a DC voltage, was done by Druyvesteijn & Penning [3]. The transformation process of a neutral gas into a conducting self-sustaining discharge is known as plasma breakdown or ignition and the corresponding voltage is called the breakdown voltage. For a self-sustaining discharge, a so-called "electron avalanche" is required. This effect is started by free electrons present in the gap between the electrodes, created by external sources such as the photoelectric effect [4]. If a voltage is applied between the electrodes, these electrons experience a body force towards the anode due to the present electric field. If the voltage between the electrodes is high enough, i.e. higher than a certain critical voltage, the electrons that move towards the anode can ionize neutral gas particles on impact, leaving a positive ion and releasing another electron. The electrons will be accelerated further towards the anode and may collide again, causing second ionizations, enhancing the process even more [4]. For more information on electron avalanches, see, for example, Raether [5]. Figure 2.1 displays a schematic representation of the electron avalanche process.

The created positive ions will be accelerated toward the cathode, resulting in an ion bombardment. These ions can cause secondary emission of electrons by impact, further contributing to the avalanche process. Other reactions that can take place include recombination and photo-emission due to excitation of atoms, which causes a glow to appear during a discharge [7].

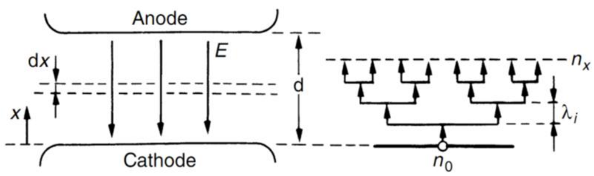

Figure 2.1: *A schematic depiction of the electron avalanche process. From Kuffel et al. [6].*

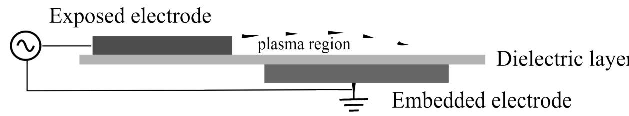

Figure 2.3: *Schematic representation of the 2D geometry of an SDBD actuator*

2.2 Dielectric barrier discharge

In this report, plasma actuators are considered. Even though gas discharges are involved in their operation, these devices function in a fundamentally different way from the DC gas discharges between two electrodes mentioned in the preceding section. The discharges involved in plasma actuation are dielectric barrier discharges (DBD).

A dielectric barrier discharge (DBD) is a discharge between two electrodes separated by a layer of dielectric material. DBD discharge devices are mostly operated in high-pressure gases. See figure 2.2 for a possible dielectric barrier configuration. The general purpose of the dielectric barrier is to limit the current and thus prevent the formation of arcs in high-pressure gases.

If such a device is driven by a DC voltage, charge carriers will accumulate on the dielectric surface - which is essentially a capacitance - and the electric field induced by that charge will counter the electric field between the electrodes. If this effect is strong enough, the potential difference across the gap will be reduced to zero, and subsequently, the discharge will cease [8] [9]. It is this self-limiting behavior that characterizes DBDs: a dielectric barrier discharge can only be sustained continuously if the applied voltage is constantly increasing, which is, for practical reasons, unrealistic. Usually, therefore, AC waveforms are used to operate DBD devices: the applied voltage then switches between positive and negative values and discharges can be started anew during each half-cycle.

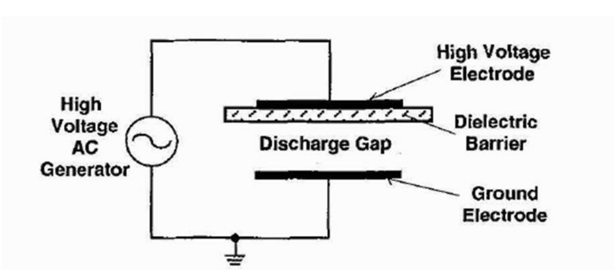

Figure 2.2: *A possible DBD configuration. From Kogelschatz et al. [8]*

The simplest type of plasma actuator is called the Single Dielectric Barrier Discharge actuator (SDBD). This is an asymmetrical dielectric barrier configuration. It consists of two electrodes, one of which is usually grounded, and a dielectric that separates them. The grounded electrode is usually embedded in the material across which flow control is required. For a schematic representation of the geometry, see figure 2.3. The idea is to induce a discharge between the two electrodes and use it to inject momentum into the surrounding fluid (usually, air).

To understand the functioning of this device in flow control, it is necessary to understand what kind of discharge is taking place. As mentioned, the waveform must realistically be of AC type if discharges are to continue to be created. However, it turns out that the induced discharge is not an AC discharge that follows the voltage, but has its own distinct spatial and temporal characteristics [9] [10].

If the applied voltage is sinusoidal in shape, then on a macroscopic scale, one would expect an SDBD discharge to behave as displayed in figure 2.4. First of all, a discharge can only be created once the voltage is past a certain critical (absolute) threshold value. This is displayed as point (a) in the figure. As long as the voltage keeps getting more negative, the counter-electric field induced by the build-up of negative charge on the dielectric will not have a large enough influence to stop the discharge; however, once the voltage is at its minimum, when $\frac{\partial V}{\partial t} = 0$, the discharges will cease (b), due to the actuator's self-limiting behavior. Subsequently, nothing will happen until the voltage is past the threshold value during the next (positive) half-cycle (c). From then on, discharges can take place as long as the voltage keeps rising, up until (d). Typical voltage amplitudes that allow for this kind of behavior are in the order of kilovolts or tens of kilovolts [9] [11] [12] [13]. As it turns out, this kind of device is capa-

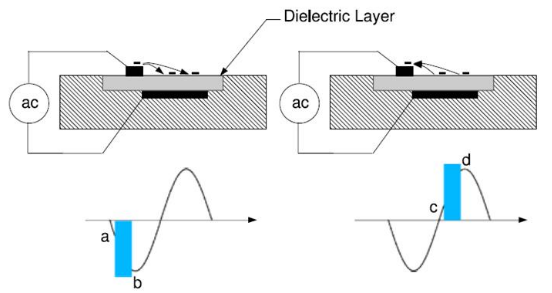

Figure 2.4: *Macroscopic prediction of DBD discharge behaviour, subject to a sinusoidal waveform. From Corke et al. [14]*

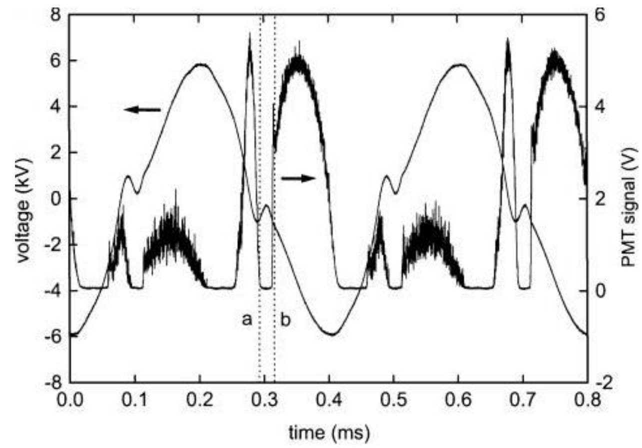

Figure 2.5: *PMT signal as a measure of plasma actuator light emission, as well as voltage across the plasma actuator, as measured by Enloe et al. [9]. The voltage frequency was 2.5 kHz. The "bumps" in the voltage, at e.g. t ≈0.1 ms, were due to an "impedance mismatch in the driving circuit", and induced an immediate discharge shutoff: a clear manifestation of the self-limiting behavior.*

ble of inducing thrust and generating wall jets when operating in still air.

This kind of "macroscopic" prediction of behavior does not yet say anything about the actual shape of the discharge occurring during periods (a)-(b) and (c)-(d). In order to determine this, Enloe et al. [9] used photomultiplier tubes (PMTs) to measure the light emission from an SDBD plasma actuator, taking this as a measure of the plasma density. The voltage across the discharge was measured as well: see figure 2.5. It can be seen in this graph that, indeed, the discharge is only active during those parts of the cycle in which the voltage was (in absolute terms) increasing and above a cricital value. It can also be seen that the strength of the PMT signal depends heavily on whether the voltage is in its positive or negative half-cycle, i.e. it appears much stronger during the negative half-cycle.

Figure 2.6 displays measurements by Enloe et al. [9] of the PMT signal and the discharge current with sub-microsecond resolution. It can be seen that the current through the discharge consists of a large number of individual short pulses. The time scale of one such current pulse appears to be in the order of microseconds or even less. The macroscopic effect, which to the eye might seem like a uniform discharge, thus consists of a huge number of individual micro discharges. In the upper graph, an asymmetry between positive half-cycle discharge (left) and negative half-cycle discharge (right) is apparent.

Pons et al. [15] measured the discharge current of an SDBD actuator as well. See figure 2.7. These measurements again confirmed that the current consists of a large number of individual micro discharges that occur only during certain portions of the waveform period.

Orlov [10] also performed light emission and current measurements on an SDBD actuator. Here, as in the study by Enloe et al. [9], the strength of the current pulses was seen to depend heavily on the cycle of the voltage.

Above a certain voltage (much higher than the breakdown voltage), the homogeneous discharges turn into streamers [12]: thin channels of ionized particles reaching from the exposed electrode towards the dielectric. One theory states that these channels grow because of photoionization: photons emitted during a local electron avalanche ionize other particles, freeing electrons that join in the initial avalanche. These electrons are able to ionize other particles, both directly and by further photoionization. These local charge distributions cause high local electric fields, comparable in magnitude to the external electric field, which make the streamer propagate at high speed towards the other electrode [7]. See figure 2.8.

Figure 2.9 displays a spanwise picture of a plasma actuator, taken at the critical voltage for the onset of streamer formation. The emission of light in thin streamers is clearly visible.

Both Enloe et al. [9] and Orlov [10] have proposed to model a plasma actuator as an electrical circuit consisting of time-dependent resistances, representing the plasma, and a number of capacitances, some constant and some time-dependent, representing the electrodes and the dielectric. Figure 2.10 shows the

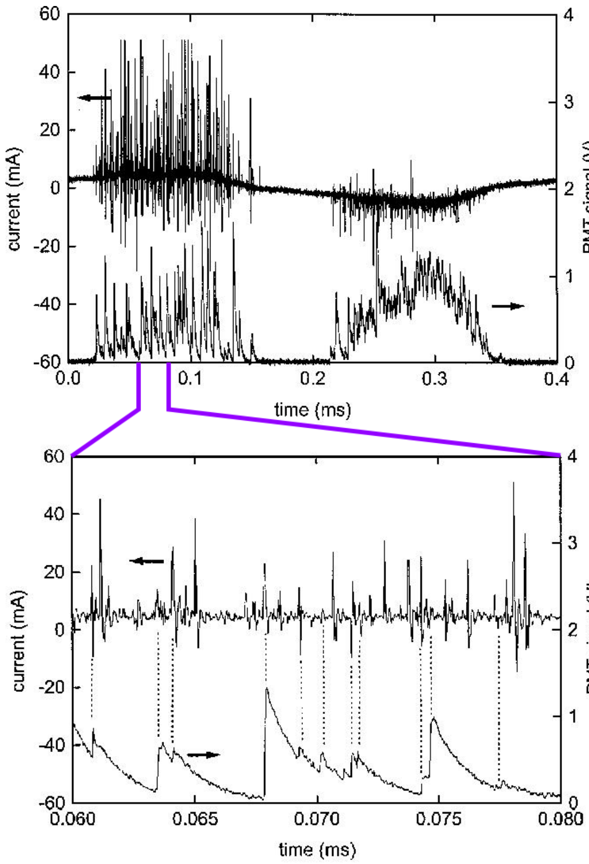

Figure 2.6: *PMT signal from plasma actuator, and current through the discharge, as measured by Enloe et al. [9] during one period of a 2.5 kHz sine waveform. In the upper plot, the range 0.0-0.2 ms corresponds to the positive voltage half-cycle, and 0.2-0.4 ms to the negative one.*

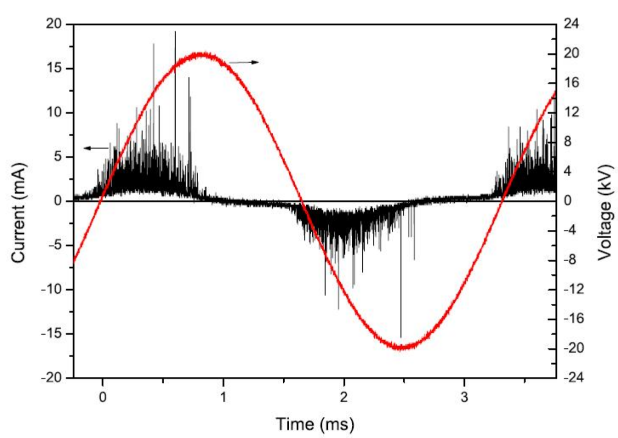

Figure 2.7: *Input voltage and discharge current due to operation of a plasma actuator, at 20 kV amplitude and a frequency of 300 Hz. Measurements from Pons et al. [15].*

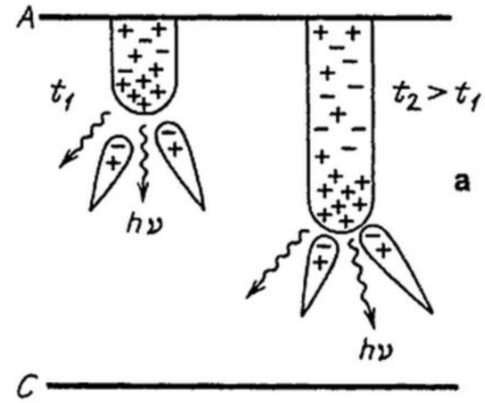

Figure 2.8: *A schematic representation of the development of streamers, a phenomenon occurring in plasma actuation. Picture from Raizer [7].*

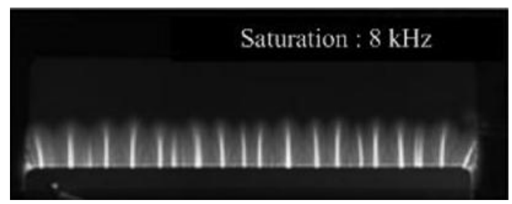

Figure 2.9: *Photo of streamer development on a plasma actuator electrode. From Thomas et al. [12].*

circuit proposed by Enloe et al. Orlov proposed to add zener diodes to the circuit to simulate the breakdown voltage. See figure 2.11.

2.3 Generation of thrust

At this point it is sufficient to note that, *somehow*, an operating plasma actuator is able to induce thrust and create wall jets in still air. While numerous simulations of plasma actuation have been performed and a number have shown good agreement with experimental results (see the later section on numerical methods), there is, to the authors' knowledge, currently no generally-accepted theory that completely explains the mechanism behind the thrust generation on a particle scale.

One might expect intuitively that, if the applied voltage is alternating, then any generated thrust should be changing direction during a voltage cycle, too. After all, particles attracted by one of the electrodes during a positive cycle will be repulsed by that same electrode during the negative cycle, and vice versa. And if that were the case, then a plasma actuator would not be an efficient flow control de-

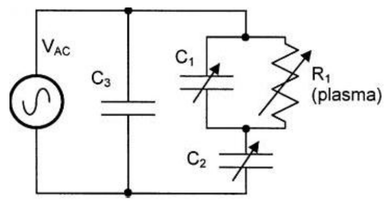

Figure 2.10: *The RC-model proposed by Enloe et al. [9]*

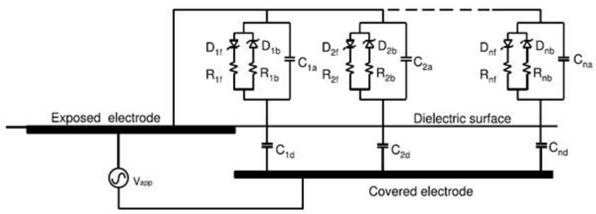

Figure 2.11: *The more complicated RC-model proposed by Orlov [10].*

vice. However, it has been found by a number of studies that the net body force induced by a plasma actuator is always in the same direction: away from the exposed electrode and towards the dielectric [9] [12]. An attempt at modeling and explaining this phenomenon has been reported by Likhanskii et al. [16]. Using the results of their model, they proposed that during positive voltage half cycles, the body force is due to positive ions heading for the dielectric, and during negative voltage half cycles it is due to negative ions heading in the direction of the dielectric. These negative ions would be formed in attachment reactions of electrons to neutral gas particles. Likhanskii et al. postulated that, while there is a countercurrent of particles heading for the exposed electrode during both half-cycles, reducing the efficiency of the actuator, the net body force is still always in the same direction [16].

2.4 Applications and optimization of plasma actuation for flow control

There is a wide range of geometrical configurations of electrodes and dielectrics of different materials that are classified as plasma actuator. Each actuator has its own design, depending on the application. In this section, the specific purpose and optimization of two types are described: the single dielectric barrier discharge (SDBD) plasma actuator introduced in the preceding section, and the plasma synthetic jet actuator (PSJA).

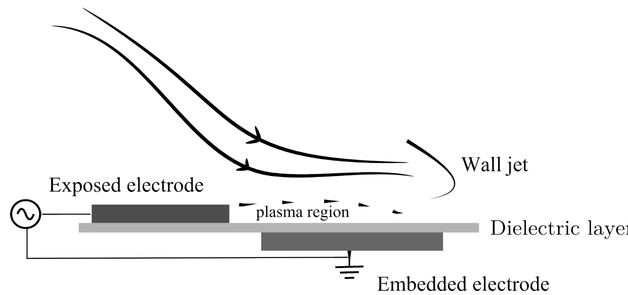

Figure 2.12: *Schematic display of the purpose of a DBD actuator: generating a wall jet*

2.4.1 Single dielectric barrier discharge actuator

As mentioned, the idea of an SDBD actuator is to induce a discharge between the two electrodes. This discharge injects momentum into the surrounding fluid, creating a wall jet which can delay boundary layer separation, an important aspect in lift and drag control. A schematic displaying the essence of SDBD operation is shown in figure 2.12.

To get an idea of the velocity field induced by a typical SDBD actuator wall jet, see figure 2.13. This figure displays results from Pons et al. [15], who measured actuator-induced velocity profiles above a dielectric flat plate in initially still air, for different horizontal positions (i.e. along the dielectric surface). Typical velocities induced in still air by plasma actuators are in the order of a few ms^{-1} [11] [17] [18] [19].

The variables which influence the performance of an SDBD can be categorized as follows: 1) the geometric parameters; 2) the dielectric material; and 3) the electrical parameters. These are discussed separately below.

Geometric parameters

The main geometric parameters that determine the performance of the plasma actuator are the size of the upper and lower electrode, the gap between the exposed and grounded electrode, and the thickness of the dielectric. See figure 2.14.

A notable study on geometric effects has been carried out by Forte et al. [11]. For a driving frequency of 700 Hz, an amplitude of 20 kV and a 2 mm thick glass plate as a dielectric, it was found that a maximum velocity in the wall jet occurred for an electrode gap width of 5 mm. It was also concluded that the grounded electrode has a maximum effective width -

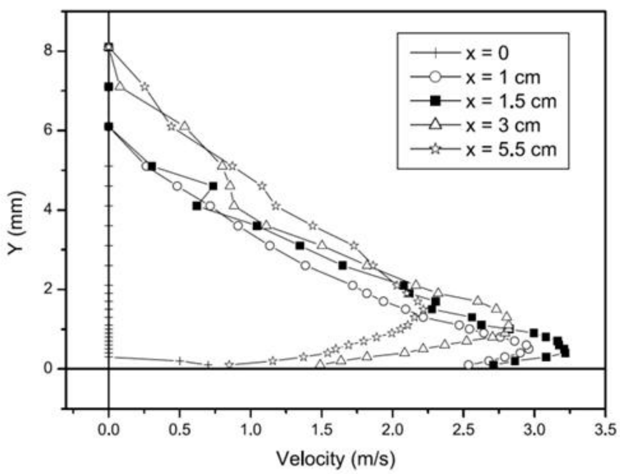

Figure 2.13: *Velocity profiles at different horizontal positions (x=0 at the edge of the upper electrode). A glass plate of thickness 4 mm was used as a dielectric. The input waveform had a driving frequency of 300 Hz and an amplitude of 20 kV. The highest velocity was seen to occur at x=15 mm. Data from Pons et al. [15].*

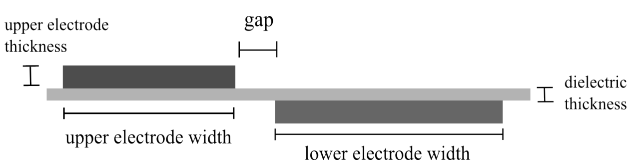

Figure 2.14: *Important geometrical parameters in SDBD actuator operation*

depending on the extent of the plasma region - beyond which, the extra width is only a waste of space. This was also mentioned by Enloe et al. [17]. The optimum width of this electrode was in this case determined to be about 20 mm. Thirdly, it was concluded that the maximum induced velocity increases when the dielectric thickness decreases, though for very thin dielectric layers the discharge becomes unstable and filamentary.

Enloe et al. [17] investigated the performance of an actuator for which the exposed electrode was a cylindrical wire instead of a strip. At dissipated power levels in the order of tens of Watts, it was found that the thinner the wire, the higher the induced thrust for a certain value of the dissipated power. A similar trend was found to apply to flat electrodes: the thinner the electrode (normal to the actuator surface), the higher the generated thrust.

Thomas et al. [12] studied the effect of the dielectric thickness on the induced body force. It was concluded that the body force increases with increasing dielectric thickness, contradicting the results found by Forte et al. [11] and Pons et al. [15], both of which indicated that decreasing the thickness is beneficial for the maximum induced velocity.

A notable type of plasma actuator is the multiple DBD, studied by Forte et al. [11]. This configuration consists of a number of SDBD actuators placed behind one another, so that each actuator can add further momentum to the flow. It was found that, with an actuator spacing of 2 cm, electrode widths of 20 cm and zero gap widths, each subsequent actuator added more velocity to the flow. After the third actuator, though, the effect became quite small due to the onset of turbulence. The maximum velocity found was 8 ms^{-1} at 25 kV amplitude and a driving frequency of 1 kHz.

Dielectric material

One common choice for dielectric material in plasma actuators is Kapton. Separating the two electrodes by Kapton has been applied in a number of studies [17] [19] [20], sometimes in the form of very thin Kapton tape. PMMA has been used by Forte et al. [11] and Balcon et al. [18]. The former used glass as well, comparing the performance of SDBD actuators using either material as dielectric. It was seen that the glass actuator induced higher maximum velocities than the PMMA actuator up to an input voltage of approximately 20 kV in amplitude.

Thomas et al. [12] studied the effect of the dielectric material on the induced body force. A comparative study between Kapton, Teflon, Delrin, Quartz and Macor was performed. The material which gave the best results was Teflon with a thickness of 6.35 mm. The main advantage of this Teflon over the popular Kapton tape was an increased support of high voltages (order-of-magnitude), which is desirable since higher input voltages appear to correspond to higher induced velocities [11]. It was also concluded that the body force increases with increasing dielectric strength and decreases with increasing dielectric constant. Again, this is not in line with the results by Forte et al. [11] and Pons et al. [15], both of which indicated that increasing the dielectric constant is beneficial for the maximum induced velocity.

Electrical parameters

In general, the electrical parameters of the applied voltage that play a role in the operation of a plasma

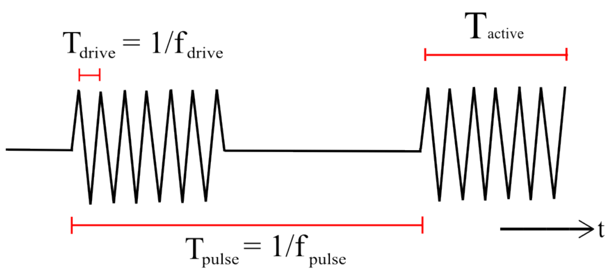

Figure 2.15: *Pulse train: driving frequency, pulsing frequency and duty cycle*

actuator are the amplitude, the waveform, the driving frequency, and, in the case of a pulse train, the pulsing frequency and duty cycle. See figure 2.15 for a clarification of what is meant by the driving frequency and the pulsing frequency. The duty cycle is the ratio of the duration of the active part of a period and the period itself: T_{active}/T_{pulse}.

Results from Thomas et al. [12] indicate that a sawtooth driving waveform, whether positive or negative, holds benefits over sinusoidal waveforms. At high voltage amplitudes - more than approximately 40 kV peak-to-peak - the thrust generated by a 2 kHz ramp signal was considerably higher than that due to sine waveforms at 1, 2, 4 and 8 kHz. For all waveforms, typical values for the power dissipation were in the order of hundreds of Watts.

Enloe et al. [9] investigated the importance of the discharge's asymmetry across the half-cycles by applying two asymmetric sawtooth waveforms between the electrodes, one with a positive ramp and one with a negative ramp. Subsequently, the thrust induced by the actuator was measured. It was found that the negative-ramp sawtooth was able to produce a higher thrust than the positive-ramp one, at the same power consumption. This was explained by noting that, from the PMT signal (figure 2.6), the plasma appeared to be much more regular during a negative half-cycle than during a positive one. Since the negative-ramp sawtooth had a higher negative-going duty cycle than the positive-ramp one, the induced plasma was more regular for the former, which was thus "more efficient in coupling momentum into the flow" [9].

Balcon et al. [18] also compared the performance of the same two kinds of sawtooth waveforms in inducing wall jets. Taking the induced velocity and the homogeneity of this velocity over the surface into account, they concluded that the sawtooth with negative ramp was likely the more appropriate to "induce homogenous and rapid airflows near the surface of an aerodynamic shape, in the boundary layer region" [18].

Forte et al. [11] found an optimum driving frequency of 1200 Hz at a fixed voltage amplitude of 20 kV for a sinusoidal waveform for their actuator. Past this frequency, the induced maximum velocity, of approximately 6 ms^{-1}, was found to display asymptotic behavior, hardly changing any more for higher applied frequencies.

An attempt at pulse frequency optimization was performed by Huang et al. [13]. Plasma actuation was applied on wind turbine blade models to control the spread of the flow separation zone occurring above the trailing edge. Here, a pulse train with a driving frequency of 5 kHz was used. By measuring the pressure distribution at a certain point above the trailing edge, it was found that the pulsing frequency f_{pulse} was optimal for separation control when the Strouhal number Sr, based on a typical separation length L_{sep} and the freestream velocity U_∞, was approximately unity:

$$Sr = \frac{f_{pulse} L_{sep}}{U_\infty} \approx 1, \tag{2.1}$$

corresponding in that case to $f_{pulse} = 114$ Hz. The same study also showed that, at equal pulse frequencies, a duty cycle of 10% was as effective as one of 50% in controlling the flow separation.

Little et al. [21] also investigated the effect of the driving frequency. In their study, the performance of an AC-driven SDBD was compared to that of a nanopulse-driven SDBD (ns-DBD). The induced wall jets were measured to be substantially weaker for the nanopulse-driven device.

2.4.2 Plasma synthetic jet actuator

A synthetic jet is a zero-net mass flux jet, i.e. a jet created out of the same fluid that surrounds it. Such a jet can be created, for example, by alternating push-suction actions on a fluid by an oscillating piston. Applications for synthetic jets are diverse. As a first example, there are possibilities for separation control and stall delay by operating jets near the leading edge of an airfoil [22] [23]. Secondly, synthetic jets can be used to produce thrust for propulsion, which can be of advantage for small and micro-aircraft [24]. Thirdly, the production of thrust by synthetic jets can potentially be applied to change an airfoil's effective angle of attack while keeping the lift constant, which essentially means a

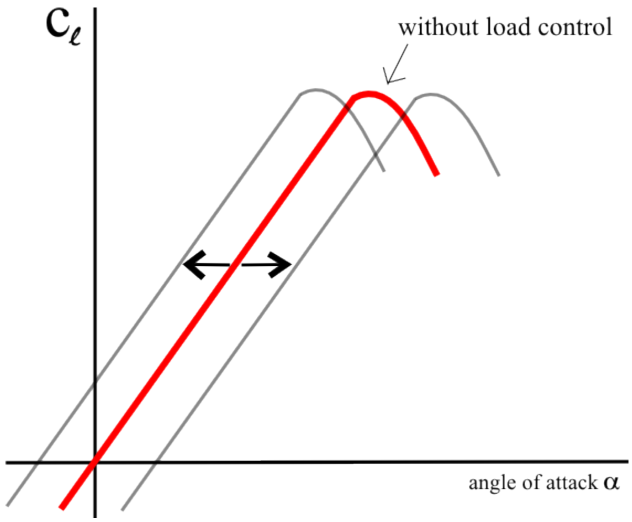

Figure 2.16: *Load control illustrated. The entire lift curve can be translated to the left or right, enabling constant lift over a range of angles of attack.*

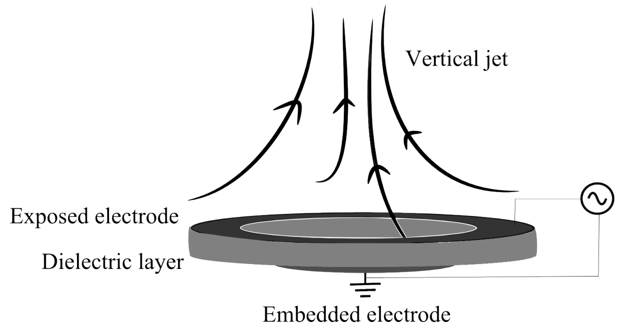

Figure 2.17: *Schematic representation of a synthetic jet created by an annular plasma synthetic jet actuator*

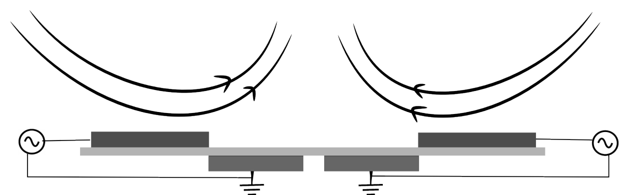

Figure 2.18: *Schematic representation of a 2D PSJA*

translation of the entire lift curve along the α (angle of attack) axis, thus enabling e.g. the same lift at lower angles of attack (a type of load control). See figure 2.16.

An overview of some methods for synthetic jet generation can be found in [25]. Some other studies focusing on the characteristics and performances of synthetic jets as possible flow control devices are described in [26], [27] and [28].

Synthetic jets can also be created by using the principle of plasma actuation. Therefore, plasma actuation is not only potentially useful for flow separation control, but also for load control.

The characteristics of SDBD plasma actuators can be used to create flow patterns other than only jets tangential to the wall. Jacob et al. [29] proposed to use two concentric annular electrodes, one exposed and one embedded, in quiescent flow, to produce tangential wall jets oriented towards the center of the configuration. See figure 2.17 for a schematic representation of this process. This kind of actuator results in a 3-dimensional jet normal to the wall [30] and is called a plasma synthetic jet actuator (PSJA).

Using the same principle, a 2-dimensional upward jet can be obtained by using two SDBD plasma actuators, consisting of rectangular strip-shaped electrodes, oriented oppositely on the same surface and operated simultaneously in quiescent air. See figure 2.18 for a schematic representation. In this case, two wall jets directed towards each other are induced by the respective actuators, which results in a jet normal to the wall that is basically 2-dimensional. (Note that a cross-section of the 3-dimensional annular configuration would give a similar figure.) Analyzing this kind of 2D-pattern can be more convenient than a 3D jet structure, for instance when using particle image velocimetry (PIV) [30] [31].

Alternatively, the two embedded electrodes can be replaced by a single one as displayed in figure 2.19. These 2D-actuators are sometimes referred to as linear plasma synthetic jet actuators (L-PSJA) [32].

A characteristic streamline plot of the flow pattern induced by PSJA operation is given in figure 2.20. It can be seen that the actuation can cause two oppositely rotating vortices to appear above the electrodes, the jet developing in the middle. Next to these main vortices, the development of secondary and even tertiary vortices closer to the actuator surface has been observed and explained [30] [33]. The experimentally observed occurrence of distinct vortex pairs has also been reproduced in numerical simulations [31].

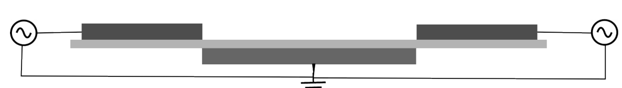

Figure 2.19: *Schematic representation of a 2D PSJA with one lower electrode*

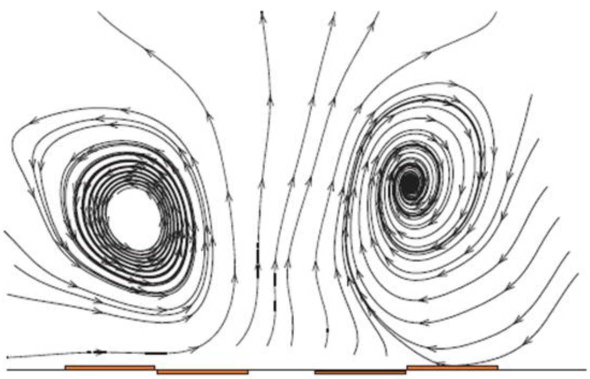

Figure 2.20: *Characteristic vortex pattern above a PSJA. Picture from Santhanakrishnan & Jacob [30].*

The main advantage of plasma synthetic jet actuation, when compared to other types of synthetic jets, is the extremely fast response time of a PSJA system. Other advantages are the absence of movable parts of any kind, their ease of mechanical construction, and their lack of any jammable opening.

As is the case with SDBD actuation devices, the performance of PSJA configurations depends on a number of parameters. See the earlier section on SDBD optimization. A number of notable results from specific research into PSJA are summarized below.

Santhanakrishnan et al. [30] used PIV to analyze the vortex structures and velocity field induced by an L-PSJA on a flat-plate in quiescent air for different pulsing frequencies of a square wave pulse train at 50% duty cycle, as well as at steady actuation (100% duty cycle). It was found that, for the highest investigated pulse frequencies, at 100 Hz, the characteristics of the induced jet started to resemble those caused during steady actuation. Pulse frequencies of 10 Hz were found to induce the highest maximum jet velocities, of the order of 1 ms^{-1}. Furthermore, the performance of the plasma synthetic jets in the presence of crossflow velocities of the same order of magnitude was investigated. The penetration depth of the jets was found to be less than 1 cm in all cases, and to decrease with increasing Reynolds number of the crossflow.

Bolitho & Jacob [33] describe a number of ways of controlling the direction and strength of a plasma synthetic jet. Firstly, applying a difference between the driving frequencies of two oppositely-oriented plasma actuators was seen to induce a difference in performance between the left and right actuator, resulting in a jet inclined towards the weaker actuator. Secondly, a difference in duty cycle also proved to be effective in adapting the jet angle. Values between 10 and 90 degrees relative to the surface normal were observed for duty cycle differences between 0 and 50%.

Bolitho & Jacob also investigated the application of a phase shift of π between the driving waveforms of each electrode pair. It was shown that, beyond a certain critical pulsing frequency, the induced jet was similar in strength to one induced at steady actuation, because the combination of frequency and phase shift was such that vortices induced by one actuator during the other's rest period, pushed upwards the vortex previously induced during the other actuator's active phase. Below this critical frequency, the induced vortices were unable to push each other upwards, instead cancelling out or not interacting at all, meaning that the induced jet strength was far smaller. All pulsing frequencies were in the range 10-700 Hz. Again, maximum velocities were of the order of 1 ms^{-1}.

2.5 Numerical methods

The focus of most modeling approaches to plasma actuation is to compute the body force applied to the charged particles in the flow. From the body force distribution, the induced jet velocities can be calculated. A few notable results are described below.

In principle, the force per unit volume acting on (charged) particles due to the operation of a plasma actuator is represented by

$$\mathbf{f} = \rho_c \mathbf{E} \tag{2.2}$$

where $\mathbf{f}$ is the force density (Nm^{-3}), ρ_c is the charge density in the plasma (Cm^{-3}), and $\mathbf{E}$ is the electric field vector (Vm^{-1}) within the plasma region[1] [17] [20]. The modeling of the operation of a plasma actuation device thus generally focuses on computing the (spatial and temporal) charge density and potential (and so, the electric field $\mathbf{E} = -\nabla\Phi$) induced by the actuator.

To give an example, Enloe et al. [17] provide a derivation of an approximate expression for the local charge density in the plasma. This formula contains the so-called Debye length, λ_D, which is the

[1] Here, it is assumed that the Lorentz force term per unit volume $\mathbf{J} \times \mathbf{B}$, with $\mathbf{J}$ the current density (Am^{-2}) and $\mathbf{B}$ the magnetic field (T), can be neglected.

characteristic length scale over which charge separation takes place (for more detailed information on the derivation, see also Appendix F):

$$\rho_c = -\frac{\epsilon_0}{\lambda_D^2}\Phi, \tag{2.3}$$

where Φ is the electric potential. This formula suggests that the electric charge density in the discharge region is linearly proportional to the local value of the electric potential. Then, the body force per unit volume in the discharge region becomes

$$\mathbf{f} = -\frac{\epsilon_0}{\lambda_D^2}\Phi\mathbf{E}. \tag{2.4}$$

When determined, this kind of force term can be added into the Navier-Stokes equations as a momentum source term.

Orlov [10] gives a detailed description of both an electrostatic model and an electric circuit-based model, the latter of which represents the plasma actuator operation in the shape of a network of resistors and capacitors. A noteworthy fact is that one type of circuit model by Orlov displayed the same correlation between the power dissipated in an SDBD plasma actuator and the applied voltage ϕ_{ext}, as has been found experimentally by Enloe et al. [9]: namely,

$$P \sim \phi_{ext}^{7/2}. \tag{2.5}$$

Also, Enloe et al. [17] and Post [20] experimentally found the same correlation between the maximum velocity induced by an SDBD actuator and the applied voltage,

$$u_{max} \sim \phi_{ext}^{7/2}, \tag{2.6}$$

hinting at a linear scaling of the maximum velocity as a function of the power dissipated by the actuator.

A less empirical, more physical and chemical model by Boeuf and Pitchford [34] takes into account the interactions between electrons, ions and neutral particles in a plasma discharge and the phenomena of drift, diffusion and recombination, computing the resulting forces. The model by Likhanskii [16], which has been mentioned, starts from similar principles and aims to provide a possible explanation of the physical processes taking place during the negative and positive half-cycles of a DBD actuator driven by a sinusoidal voltage, and of the direction of the body force in such a device. Another example of a model based on interactions at the molecular scale and mass transfer principles has been described by Jayaraman [35].

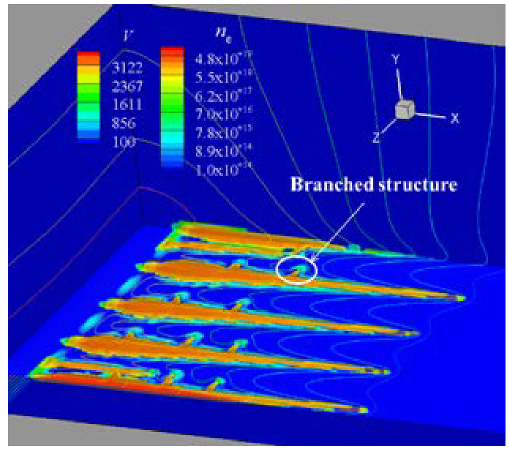

Figure 2.21: *An example of streamer development as simulated by the model of Nishida et al. [36]. Shown are the electron number density and equipotential lines.*

A notable recent model was developed by Nishida et al. [36]. This 3-dimensional simulation models the shape of the microdischarges on an SDBD plasma actuator using molecular-scale relations. The model replicates a branched structure of gas discharges from the exposed electrode on a time scale in the order of nanoseconds. When small irregularities were added on the modeled upper electrode surface, this was seen to have an impact on the discharge locations due to strong local potential gradients at these points. See figure 2.21.

Suzen et al. [37] describe a phenomenological model, which was developed for SDBD actuators, but has also been adapted to replicate PSJA behavior by Santhanakrishnan et al. [31]. In that study, the streamline and vorticity plots as well as axial velocity distributions obtained from numerical simulations were compared to experimental results obtained using PIV. The numerical method was able to "reasonably" replicate velocity and vorticity structures near the actuator.

Another approach by Shyy et al. [38] is based on a linear approximation of the electric field distribution around the electrode configuration of an SDBD actuator. This rather crude model was used by Liu et al. [39] to simulate the jet formation by a PSJA configuration and was able to replicate the formation of primary vortices and the development of a jet in between.

A more comprehensive summary of approaches used in modeling the body force and flow field induced by the operation of plasma actuators can be found in [14] and in [40].

2.6 Research focus

This study focuses on experimentally determining the velocity profiles induced by a linear PSJA device in quiescent air at different pulsing frequencies and different duty cycles using PIV. An optimization study with regard to the pulsing frequency and duty cycle has been performed. In addition, a numerical simulation of PSJA operation in quiescent air has been performed for comparison to the obtained experimental results.

Chapter 3

Experimental setup

This chapter describes the experimental setup used in this study. Firstly, the plasma synthetic jet actuator designs that have been used are described. Secondly, the operating hardware of the actuator is explained. Thirdly, an overview is given of safety measures taken in the experiments. Fourthly, the method for PIV measurements is described. Finally, the conducted measurement series are detailed.

3.1 Actuator construction

All experiments were performed with linear plasma synthetic jet actuators (L-PSJA, see section 2.4.2). Figure 3.1 shows the dimensions of the actuator design that was used throughout this study, and figure 3.2 shows a photo of one of the used actuators.

In total, three actuators of this design were constructed.

Dielectric material

As dielectric material, plates of Duran glass with dimensions 200 mm x 100 mm x 2 mm were used. Duran glass has a dielectric constant of approximately 4.6 and a transformation temperature of 525°C[1]. It is beneficial to use a dielectric material that is able to withstand the temperatures that typically occur in a plasma actuator discharge. It has, for example, been mentioned by Forte et al. [11] that using a too thin actuator can result in strong local heating, and therefore in mechanical damage to the actuator. The choice for Duran glass was primarily based on its relative durability at high temperatures when compared to Kapton tape, which has been used in earlier studies in this group but proved unreliable due to heating problems.

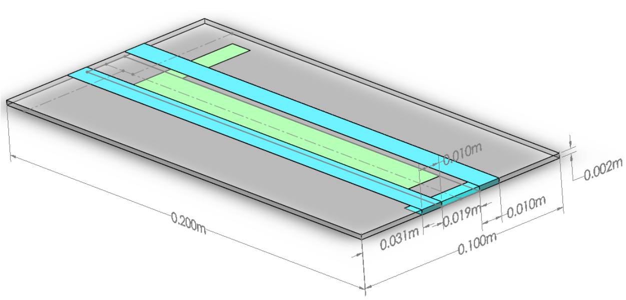

Figure 3.1: *The dimensions of the dielectric and the electrodes as used in the PSJA construction. The upper electrodes are displayed in blue, the lower electrode in green.*

Upper electrodes

The attachment of the upper electrodes to the dielectric is crucial in the construction of plasma actuators. The difficulty lies in attaching a good conductor (the electrode) to an insulator (the dielectric), which makes welding or a similar process very difficult. For this study, two options of glueing the electrodes to the glass were used.

The first option, used on two of the three actuators, was glueing non-adhesive copper strips of size 200 mm x 10 mm to the glass. The second option, applied on the third actuator, was using adhesive Advance AT526 copper tape strips of the same size.

UV-Klebstoff MV 760 was used to glue the non-adhesive copper strips, which had a thickness of 0.05 mm, to the glass. This glue hardens in UV-light and can resist temperatures of up to 150°C. The thickness of the layer of glue is listed as between 0.08-0.5 mm.[2]

[1]The data sheet for Duran glass can be found online at `http://www.duran-group.com/en/about-duran/duran-properties.html`

[2]The data sheet for the glue can be found on `http://www.bohle-group.com/shop/media/Online/PDF/DE_MV%20760.pdf`

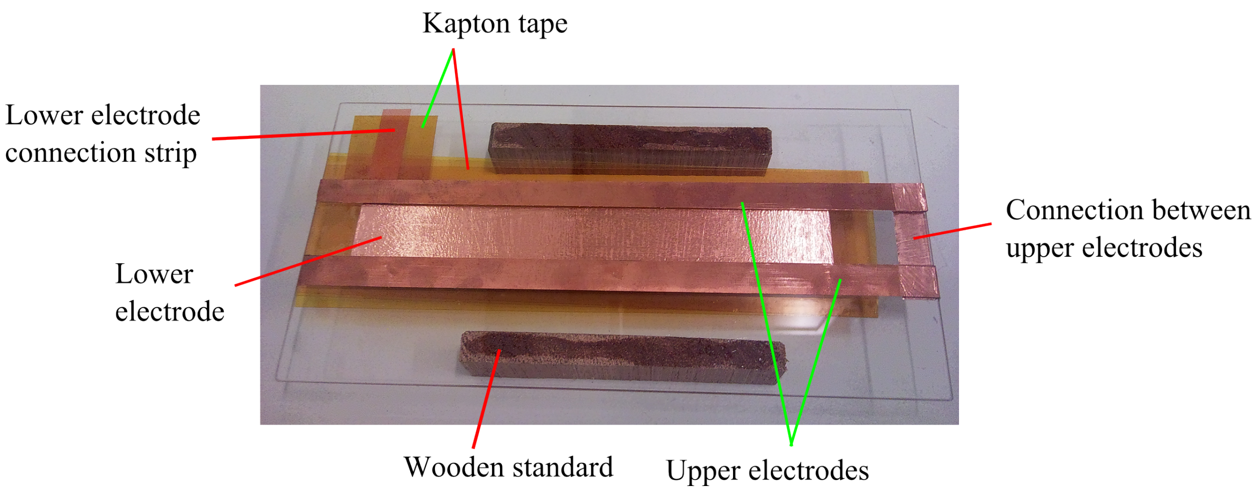

Figure 3.2: *Top view of one of the used actuators. Green arrows are used to indicate parts on the upper surface, red ones for the lower surface.*

The Advance adhesive copper tape can resist temperatures of up to 155^{o}C. One layer has a thickness of 0.035 mm.[3] A major advantage of this tape is that it can be replaced easily, making it possible to keep the actuator "in good shape" by replacing the upper electrodes if they turned out to get damaged during measurements.

Two small strips of adhesive copper tape, each connected to one upper electrode, were folded around to the other side of the glass plate. Here, these two strips were connected by another strip of copper tape. In this way, a connection point for external wires was provided such that the two electrodes could be operated in parallel.

Lower electrode

On the lower side of the plate, an electrode of size ±155 mm x 19 mm, made from adhesive copper tape, was located, so that the horizontal gap distance between the upper and lower electrodes was zero. The lower electrode was encapsulated in dielectric Kapton tape to shield it from the environment, thus preventing discharges on the lower side of the actuator. One small strip of copper tape, connected to the electrode and oriented perpendicularly to it, extended out from under the Kapton tape to act as a connection point for external wires. A small strip of Kapton tape was placed directly above it on the top surface of the glass, to prevent dielectric barrier discharges from an upper electrode to this connection strip.

[3]See also `http://www.advancetapes.com/products/markets/52/page1/87.html`

3.2 Hardware

A PSJA has to ionize the surrounding air in order to induce ionic wind. Typical plasma actuators operate at voltage amplitudes in the order of kilovolts or tens of kilovolts (see paragraph 2.2). In this study, a Minipuls 4 high voltage generator was used to produce the required voltages for inducing discharges in air. The Minipuls 4 can transform low voltage waveforms with a driving frequency in the range of 5-20 kHz to high voltage waveforms with amplitudes of up to 20 kV peak.

A Power Supply Voltcraft PS 3620 was used to provide a DC voltage as input for the Minipuls 4. A self-made LABView program and NI-DAQmx hardware were used as external waveform generator to set the waveform characteristics - driving frequency, pulse frequency, amplitude and duty cycle - as a control input for the Minipuls 4. See Appendix B for a more detailed description of the program.

Via the copper strip that connected the two upper PSJA electrodes, and the lower electrode connection strip, the actuator was connected to the Minipuls 4. The lower electrode was grounded. The output waveform of the Minipuls 4 could be checked using a LeCroy high-voltage probe (1000x attenuation) and a Tektronix TDS 2004B oscilloscope.

See figure 3.3 for a schematic overview of the setup.

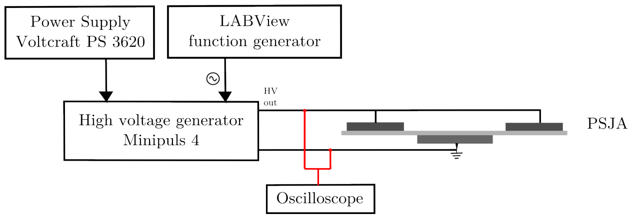

Figure 3.3: *Schematic drawing of the hardware of the setup*

3.3 Safety

The experiments have been performed inside a cabinet at ambient temperature and pressure. The cabinet had a grounded metal frame and transparent plastic windows on all sides, and could be opened on one side with a sliding door. Its dimensions were 0.55 m x 1.19 m x 0.66 m. For the experiments, a PSJA was placed in the cabinet and connected to the output wires of the Minipuls 4.

Operation of a PSJA was found to produce ozone. When a PSJA was operated for a few minutes during preliminary experiments, the ozone concentrations within the cabinet were found to be much higher than the typically allowed limit exposure value[4] of 0.05 ppm. To ensure an ozone concentration within safe limits, a NoZone® Ozone Scrubber was installed to remove ozone from the air in the cabinet in case of a too high concentration. The scrubber was connected to the cabinet by means of two tubes, so that, when operational, it drew air from one side of the cabinet and deposited the scrubbed air on the other side. In this way, air circulation for ozone depletion was ensured. The scrubber was only operated inbetween measurements, to ensure that the induced air circulation did not interfere with the velocity field measurements and that no fog, used for PIV measurements, was drawn into the scrubber.

In addition to the scrubber, a C-30ZX Ozone Monitor and Controller was used to measure the ozone concentration within the cabinet. As soon as the ozone concentration became too high, a signal was provided to a Magnet-Schultz magnetic shotbolt to lock the cabinet's sliding door.

Through an Euchner Safety Switch, the Power Supply Voltcraft PS 3620 (and with it the Minipuls 4) was automatically shut off as soon as the sliding door was opened.

See also Appendix A for pictures of the setup.

[4]See, for example, `http://www.ozonetech.com.sg/UploadedImg/File/Safe%20Ozone%20levels.pdf`

3.4 Particle Image Velocimetry

To map the velocity fields induced by the plasma synthetic jet actuators, particle image velocimetry (PIV) has been used. In this case, a Lasiris™ Class 3B laser of 665 nm was used for producing a 2D laser sheet. The assumption was made that the induced flow fields would have strong 2-dimensional characteristics due to the symmetry of the actuator design, and therefore could be adequately visualized using PIV.

As seeding particles, fog droplets created from the fog generator SAFEX Nebelgerät 2005 were injected into the above-described cabinet through a lockable tube in one of the cabinet walls. The seeding particles, created from Inside Nebelfluid Blitz/Reflex, are water-based droplets and have a size of $\sim$1 μm. After injecting the fog, the cabinet was sealed off and the fog was allowed to disperse uniformly in the cabinet before measurements were performed.

Recordings of the flow field directly above an operational PSJA have been performed with a Kodak EktaPro CR Imager Model 2000 camera and Motion Central software. The recordings were performed at a rate of 60 fps and a resolution of 512 x 384. Analysis of the raw data was performed with MATLAB and the PIV software PIVlab 1.31.[5]

See also Appendix A for pictures of the operational setup.

3.5 Measurement series

In the measurements, square waveforms generated in LABview were used as input for the Minipuls 4. The used driving frequency was 13 kHz, which had been found to be the resonance frequency of the system (Minipuls 4 plus actuator), at which the strongest discharge was induced, during earlier studies in this group. The pulse frequency and duty cycle were independently varied to investigate the behaviour of a PSJA as a function of these two parameters.

It turned out that not all combinations of pulse frequency and duty cycle values could be used with the current setup, because of distortions and/or limitations induced by the Minipuls 4. See Appendix B for a detailed explanation. Usable values for pulse frequencies were found in the range between 30 Hz and 70 Hz. Usable duty cycle values were found in the range 20% to 65%.

[5]PIVlab 1.31, by W. Thielicke & E.J. Stamhuis, is available for download on `http://www.mathworks.com/matlabcentral/fileexchange/27659`.

Due to the TTL logic at the control input of the Minipuls, it was not trivial to keep the average amplitude of the Minipuls 4 output signal constant during measurements in which the duty cycle was varied. For these measurements, the amplitude of the signal generated in LABview had to be calibrated in order to achieve Minipuls 4 output voltage values that were (approximately) constant across the duty cycle range. For a description of the used procedure, see Appendix B.

Prior to the measurements, the actuators were first tested for durability. The exact same waveform was applied 5 times in sequence, with 30-minute intervals, and the induced flow field was recorded with PIV.

The durability of the first actuator, with non-adhesive copper strips, was tested at 30 Hz pulse frequency and 50% duty cycle.

The durability of the second actuator (identical in design to the first) was tested at 30 Hz pulse frequency and 20% duty cycle. In this way, the effect of duty cycle on durability could be investigated.

The durability of the third actuator, with Advance adhesive copper tape as upper electrodes, was tested at 30 Hz pulse frequency and 50% duty cycle. In this way, the effect of using adhesive copper tape for the upper electrodes instead of non-adhesive copper strips could be investigated.

It turned out that the actuators with non-adhesive copper strips only lasted for 1 to 2 operations of $\sim$30 seconds each, after which their performance decreased considerably and the discharges became asymmetrical due to uneven damage to both electrodes. More detailed results of the durability tests are given in Appendix C.

The actuator design with adhesive copper tape as upper electrode material lasted for about 5 operations before its performance, too, decreased due to damage to these electrodes. However, the measurement series regarding pulse frequency and duty cycle could be performed without problems by replacing the upper electrodes after each measurement. In this way, each measurement was performed with an undamaged actuator of presumably the same quality.

A description of the exact protocol for these measurement series and their analysis in PIVlab 1.31 is given in Appendix D. The experimental results are discussed in chapter 4.

Chapter 4

Experimental results

This chapter describes the results obtained from the experiments and the subsequent analysis.

Figure 4.1 shows the definition of the coordinate system axes as used here.

4.1 Methodology

Two sets of measurement series have been performed. In the first, the PSJA input waveform pulsing frequency was varied between 30 Hz and 70 Hz at a constant 50% duty cycle. In the second, the duty cycle was varied between 20% and 65% at a constant 50 Hz pulsing frequency.

For each chosen value of the applied waveform pulsing frequency or duty cycle, a 2046-frame recording (34.2 seconds) of the flow field directly above the PSJA was made. From the second half of every recording, a set of 100 subsequent frames (spanning 1.67 seconds) was taken for analysis. PIV analysis was then performed with PIVlab 1.31 to compute the distribution of the vertical velocity in the recorded region for every pair of subsequent frames.

From each vertical velocity distribution corresponding to one pair of subsequent frames, the maximum upward velocity in the region above the actuator was extracted. The mean of all maximum vertical velocities, here called $\overline{v_{max}}$, was recorded as a function of the pulsing frequency and of the duty cycle.

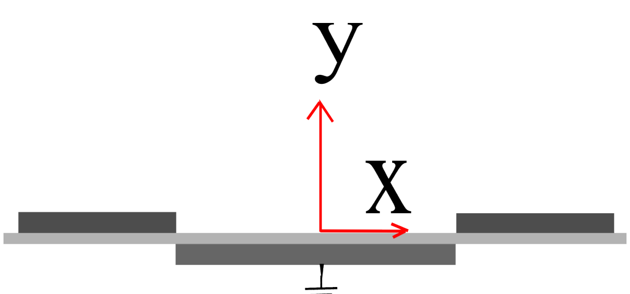

Figure 4.1: *The coordinate system within a recorded frame (not to scale) as used in the analysis. The vertical coordinate y is zero at the actuator surface; the horizontal coordinate x is zero in the middle of the actuator.*

The 99 distributions of the vertical velocity, $v(x, y, t)$, were also averaged to obtain one time-averaged distribution, $\overline{v}(x, y)$, for every value of pulsing frequency and duty cycle. From this average distribution, the following data was extracted:

1. The maximum vertical velocity along x in the average distribution, here called $\overline{v}_{max}(y)$, as a function of the vertical distance y from the actuator, for all investigated values of pulsing frequency and duty cycle;

2. The averaged vertical velocity flux per meter span above the actuator surface, defined as $Q(y) = \int \overline{v}(x, y)\partial x$, as a function of y for all investigated values of pulsing frequency and duty cycle. This quantity gives an indication of the net amount of mass displaced above the PSJA - e.g. flowing towards it (negative Q) or from it (positive Q).

The error estimation for $\overline{v_{max}}$ was performed by computing the standard deviation of each set of maximum velocities.

The average distribution $\overline{v}(x, y)$ contained a large uncertainty due to the fact that the induced turbulent jets had a very different shape from frame to frame in many cases. This uncertainty was therefore also present in the $\overline{v}_{max}(y)$ and $Q(y)$ data sets. To reduce variations within these data sets, an Rloess filter of 10 data points was applied to the plots.

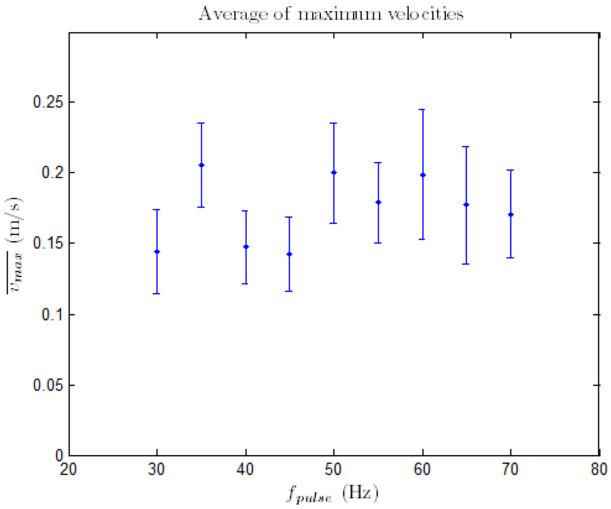

Figure 4.2: *$\overline{v_{max}}$ as a function of pulsing frequency at 50% duty cycle.*

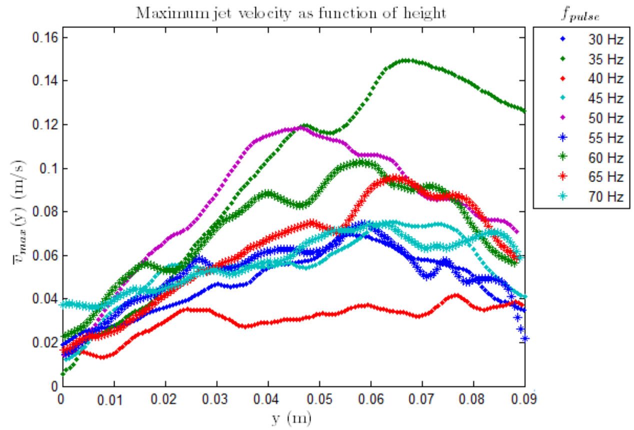

Figure 4.3: *Maximum vertical velocity in the time-averaged vertical velocity distribution as a function of distance above the actuator, for all investigated pulsing frequencies. The actuator surface is situated at $y = \sim 0$ m.*

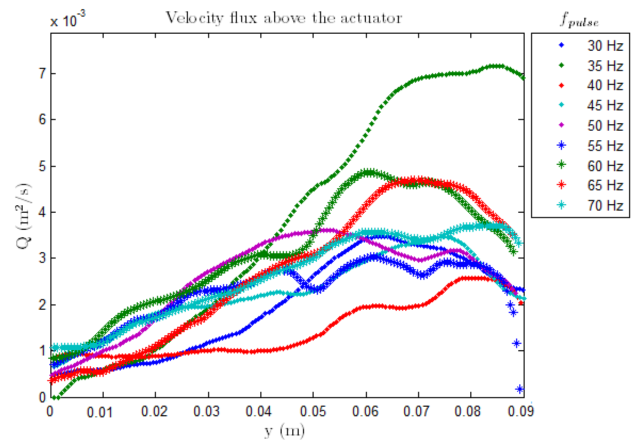

Figure 4.4: *Vertical velocity flux above the actuator, computed from the time-averaged vertical velocity distribution, as a function of distance above the actuator, for all investigated pulsing frequencies. The actuator surface is situated at $y = \sim 0$ m.*

4.2 Results for pulse frequency series

Pictures of all recorded time-averaged vertical velocity profiles $\overline{v}(x, y)$ in the pulse frequency series are given in Appendix E.

The plot in figure 4.2 displays the found values of $\overline{v_{max}}$ as a function of pulsing frequency.

The values for $\overline{v_{max}}$ are all in the range between 0.11 ms^{-1} and 0.24 ms^{-1} (including standard deviations). From the graph, it appears that the maximum vertical velocity induced by the actuator shows no significant dependence on the pulsing frequency in the investigated range at 50% duty cycle. It must be noted here that changing the pulsing frequency does not alter the total energy input into the actuator, unlike changing the duty cycle.

It is also noteworthy that Santhanakrishnan et al. [30] did find a significant dependence of PSJA performance on pulsing frequency in the range 1 Hz to 100 Hz at 50% duty cycle, although it must be mentioned that the actuator design and other electrical parameters in that study were not identical to those used here.

A plot of the maximum vertical velocity in the average jet along lines of constant y, $\overline{v}_{max}(y)$, is given in figure 4.3 for all investigated pulsing frequencies. Here, too, no dependence on pulsing frequency is apparent. It is seen that in all cases except one, the maximum vertical velocity in the time-averaged jet appears in the range between 50 mm and 80 mm above the actuator.

However, the average vertical jet velocities are still seen to vary greatly across the investigated f_{pulse}-range. The average spatial structure of the jets also exhibited significant differences across this range, as can be seen in the $\overline{v}(x, y)$-plots in Appendix E. See also section 4.4 and chapter 6 for a further discussion on this matter.

A plot of the upward velocity flux $Q(y)$ for the investigated pulsing frequency values is given in figure 4.4. The maximum values of $Q(y)$ lie in the range between 60 mm and 90 mm in all cases except one, and all maximum values are between 0.003 m^{3}s^{-1} and 0.007 m^{3}s^{-1} per meter span.

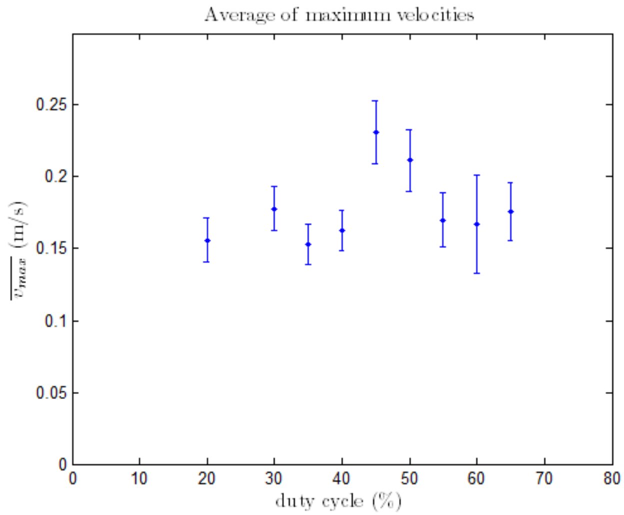

Figure 4.5: *$\overline{v_{max}}$ as a function of duty cycle at 50 Hz pulsing frequency.*

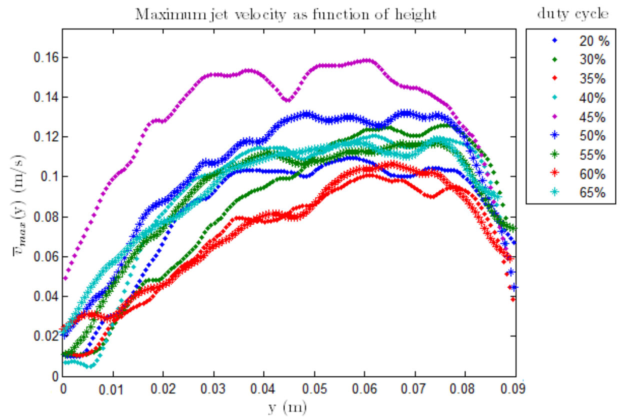

Figure 4.6: *Maximum vertical velocity in the time-averaged vertical velocity distribution as a function of distance above the actuator, for all investigated duty cycles. The actuator surface is situated at y = ∼0 m.*

4.3 Results for duty cycle series

Pictures of all recorded distributions of the time-averaged vertical velocity $\overline{v}(x, y)$ in the duty cycle series are given in Appendix E.

The plot in figure 4.5 displays the found values of $\overline{v_{max}}$ as a function of duty cycle.

The values for $\overline{v_{max}}$ are all between 0.13 ms^{-1} and 0.25 ms^{-1} (including standard deviations). No clear dependence on duty cycle appears from this graph; the velocities at high (> 55%) duty cycle are in the same range as the velocities at low (< 35%) duty cycles in the plot. This appears to be in agreement with the claim by Huang et al. [13] that a duty cycle of 10% is as effective as one of 50% in controlling flow separation at the trailing edge of a wind turbine blade model with an SDBD plasma actuator.

A plot of the maximum vertical velocity in the average jet at each y, $\overline{v}_{max}(y)$, is given in figure 4.6 for all investigated duty cycles. It is seen that in each case, the largest value is reached between 50 mm and 80 mm above the actuator surface, as in the pulse frequency series. Again, no significant difference between the smallest and the largest duty cycle values is present.

A plot of the upward velocity flux $Q(y)$ for the investigated duty cycle values is given in figure 4.7. The flux attains its maximum value in the range between 50 mm and 80 mm in all cases. All maximum values of $Q(y)$ lie in the range 0.003 $\mathrm{m}^3\mathrm{s}^{-1}$ to 0.007 $\mathrm{m}^3\mathrm{s}^{-1}$ per meter span, as in the pulse frequency series.

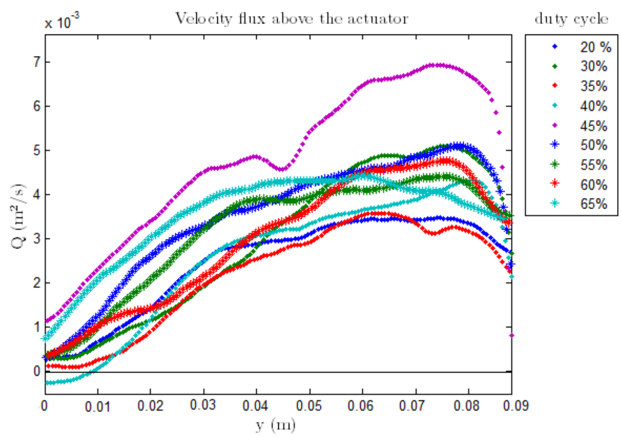

Figure 4.7: *Vertical velocity flux above the actuator, computed from the time-averaged vertical velocity distribution, as a function of distance above the actuator, for all investigated duty cycles. The actuator surface is situated at y = ∼0 m.*

4.4 Jet steadiness

As can be observed from the pictures given in Appendix E, the average spatial structures of the jets differ greatly across the measurements, both in direction and in width. To investigate the temporal steadiness of the jets further, scatterplots of the vertical velocity as a function of x, at a constant value of y, using all 99 velocity distributions belonging to one 100-frame recording, can be constructed.

Figures 4.8, 4.9 and 4.10 provide three examples of these plots. These examples have been chosen because they illustrate the different kinds of actuator

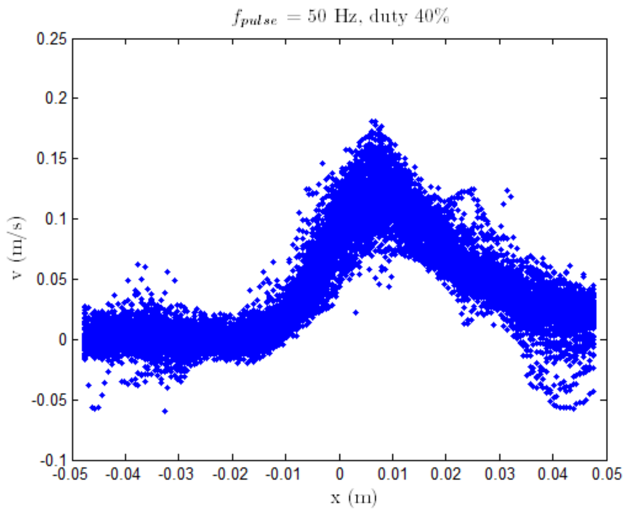

Figure 4.8: *Scatterplot of the vertical velocity above the actuator at the y-value corresponding to the maximum velocity in the time-averaged distribution, at f_{pulse} = 50 Hz and 40% duty cycle.*

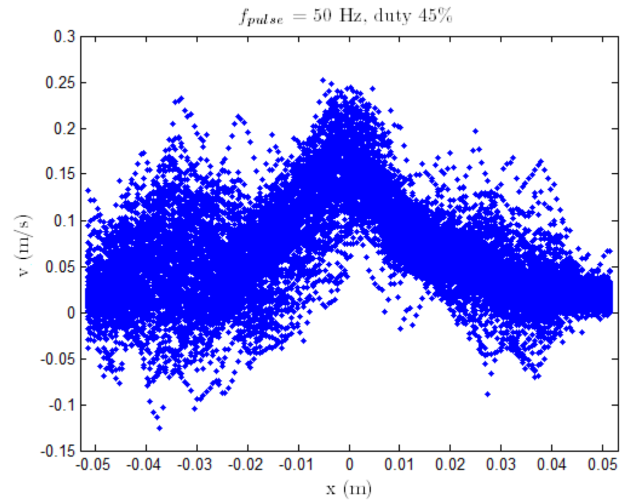

Figure 4.9: *Scatterplot of the vertical velocity above the actuator at the y-value corresponding to the maximum velocity in the time-averaged distribution, at f_{pulse} = 50 Hz and 45% duty cycle.*

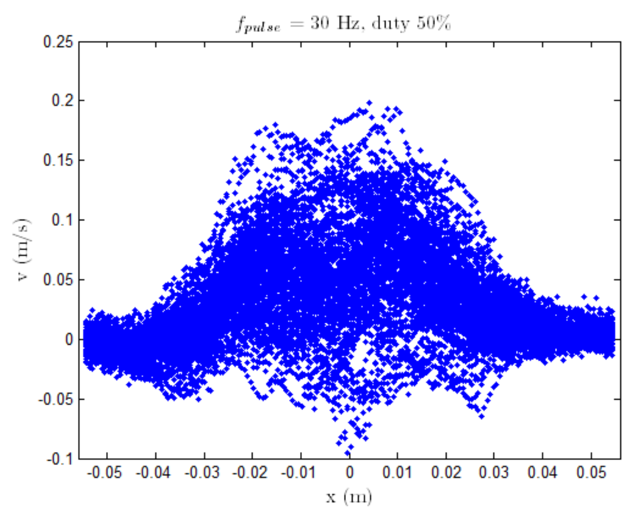

Figure 4.10: *Scatterplot of the vertical velocity above the actuator at the y-value corresponding to the maximum velocity in the time-averaged distribution, at f_{pulse} = 30 Hz and 50% duty cycle.*

behaviour observed with respect to steadiness. Here, the constant value of y has in each case been chosen to be that at which the maximum value in the time-averaged velocity profile occurred (see figures 4.3 and 4.6 as well as Appendix E).

Figure 4.8 shows the most steady example observed, at 40% duty cycle in the duty cycle series. All velocities appear to have remained within a range of about 0.05 ms^{-1} at each value of x, and it is clearly visible that the location of the jet was at basically the same horizontal position in almost each of the 99 velocity distributions.

Figure 4.9 shows an example in which the velocity at each x had a larger bandwidth in time. This was observed at 45% duty cycle in the duty cycle series. Occurrences of highly-deviating velocities can be seen on both sides of the jet. However, the location of the main jet is still clearly visible by the "bump" in the middle.

Figure 4.10 shows an example of the least steady kind of jet observed. This particular example was observed at 30 Hz pulsing frequency in the pulsing frequency series. Here, the location of the main jet is not at all clear; rather, there is a large region within which the jet appears to have shifted in orientation during the 1.67 seconds that the analyzed frames represent. Vertical velocities within a bandwidth of more than 0.20 ms^{-1} occurred in this region. In cases like this, it seems that the behaviour of the actuator is very unpredictable even within a time scale of 1.67 seconds. This also implies that if 100 different frames had been taken for analysis of this measurement, the average jet would likely have looked markedly different.

See chapter 6 for a further discussion of this unpredictability.

Chapter 5

Numerical results

Numerical simulations have been performed to see whether these could replicate the behavior observed in the experiments. The method used here is the one proposed by Suzen et al. [37]. As was mentioned in chapter 2, this is a phenomenological method which does not describe the actual physics behind plasma actuation. However, it has the advantage that it decouples the charge density in the discharge region and the electric field, thus reducing computational time and effort.

The model was initially developed for analysis of SDBD actuators. However, it can be used for modeling of PSJA actuators [31]. In essence, the simulation procedure is as follows:

- It is assumed that the potential between the electrodes can be separated into an external part (the applied voltage) and an internal part (due to charge separation).
- The externally applied voltage between the actuator electrodes is modeled by setting a finite-value potential as boundary condition on the upper electrodes, and zero potential on the lower one.
- It is assumed that the charge distribution in the region between the electrodes is governed by the value of the internal potential, which is due to the charge on the walls. It is solved for by setting a boundary value on the lower electrode and solving Maxwell's equations.
- The resulting charge density is multiplied with the external electric field (assuming the electric field due to charge on the walls is negligible) to obtain the body force, which is inserted as body-force term into the Navier-Stokes equation.

In this study, the main equations from the model of Suzen et al. have been implemented in COMSOL 4.2a, along with the specific geometric parameters used in the experimental study described in chapter 3.

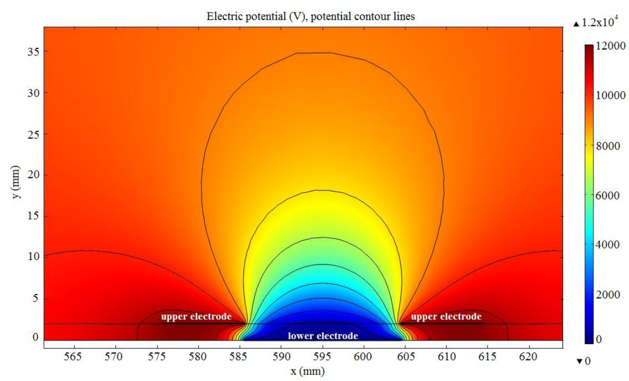

Figure 5.1: *The potential close to the actuator electrodes*

A detailed overview of the assumptions in the model, the governing equations, the boundary conditions and constants specific for this study, the geometry of the problem, and the specific COMSOL settings can be found in Appendix F.

5.1 COMSOL results

Since the simulations were performed with a DC voltage as boundary condition on the upper electrodes (see Appendix F), the resulting potential and electric field are time-independent. The potential in the air and dielectric domain close to the electrodes are presented in figure 5.1. The resulting electric field is displayed in figure 5.2. It can be seen that the electric field is strongest at the edges of the electrodes.

The charge density in the air domain, which, as mentioned, is decoupled from the electric field, is displayed in figure 5.3.

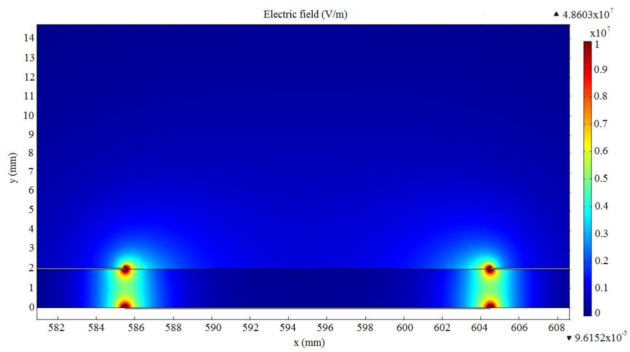

Figure 5.2: *The electric field close to the actuator electrodes*

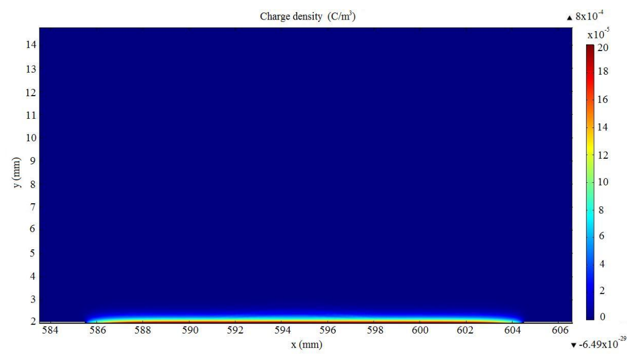

Figure 5.3: *The charge density on the dielectric surface between the upper electrodes*

The multiplication of the charge density and the electric field yields the force per unit volume in the air domain. A plot of the volume force density at the left electrode is given in figure 5.4. The maximum value of the volume force density is about 720 Nm^{-3}.

The volume force density was implemented in the Navier-Stokes equation. The initial situation was set to be a quiescent environment with zero velocity everywhere. Applying the volume force resulted in a time-dependent flow that eventually becomes steady if the simulation is run for a sufficiently long time. Wall jets formed at both electrodes at $t = 0$ and met in the middle, creating an upward jet that developed in height until the steady situation was reached. Primary vortices developed on both sides of the jet and moved upwards until the steady situation was reached, in which they occupied most of the air domain. The pictures hereafter are taken at the final time value of the simulation (t = 200 s), which is representative for the steady situation.

In figure 5.5, the streamlines in the entire air domain are displayed. The velocity in the bulk of the vortices is in the order of millimeters per second.

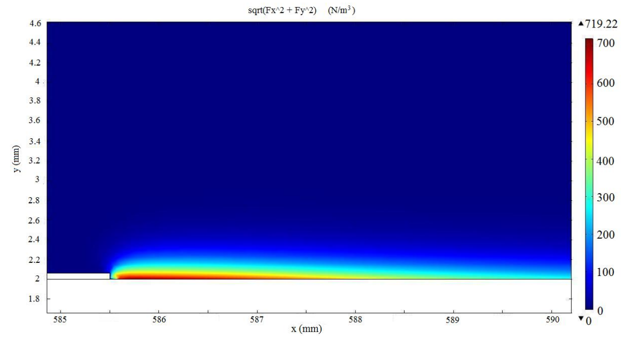

Figure 5.4: *The volume force next to the left upper electrode*

Figure 5.6 shows a close-up of the jet directly above the actuator. The maximum velocity, induced right next to both electrodes, is about 0.27 ms^{-1}. In the vertical jet, the velocity is about 0.1 ms^{-1}.

5.2 Analysis

In order to extract more detailed information from the plots, analysis with MATLAB was performed.

Jet velocity

The upward velocity within the main jet decreases with the vertical distance above the actuator y. Figure 5.7 shows a plot of the maximum vertical velocity inside the central jet versus the vertical distance above the actuator. For low values of y, this velocity decreases rapidly. At higher y values, this decrease slows down as the sides of the primary vortices start to constitute a part of the jet, as is clear from figure 5.5. At the heights at which the vortices swirl away to the sides, the jet dies out and the vertical velocity reduces to zero.

This velocity profile clearly differs from the experimentally found profiles of $\overline{v}_{max}(y)$ (see figure 4.3 and 4.6), where velocities were found to attain their largest values at approximately 50 mm to 80 mm above the actuator surface in nearly all cases.

Jet flux

Another quantity in describing the jet characteristics is the vertical velocity flux per meter span $Q(y)$ in the region above the actuator, as introduced in chapter 4.

Two plots of the flux versus y are given in figure 5.8, which covers the complete range of y-values in the simulation, and figure 5.9, which is zoomed in

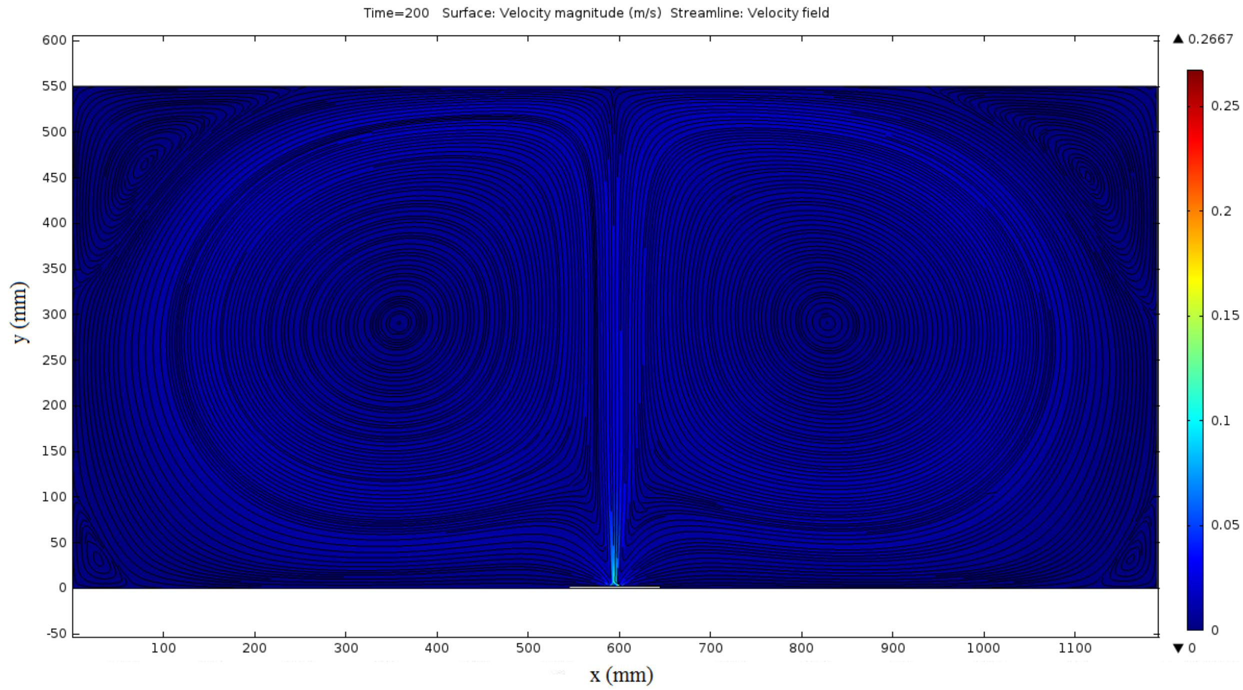

Figure 5.5: *Primary vortices form on both sides of the vertical jet*

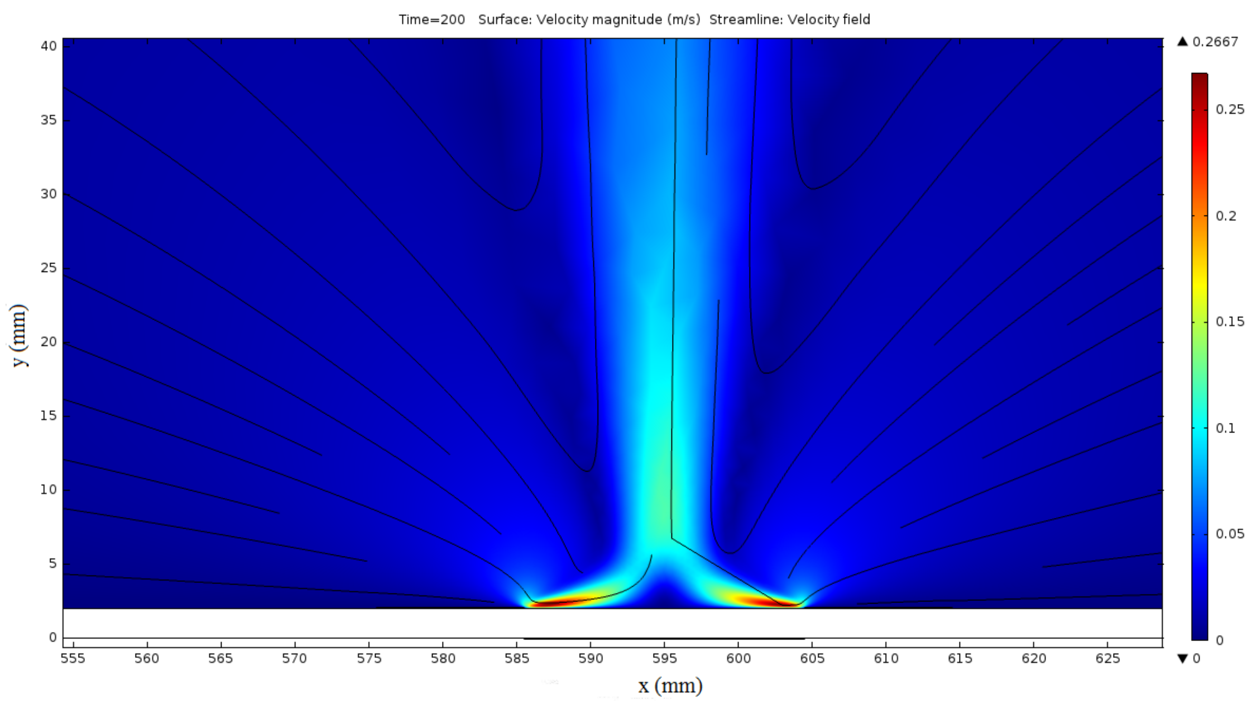

Figure 5.6: *Close-up of the velocity distribution directly above the dielectric surface*

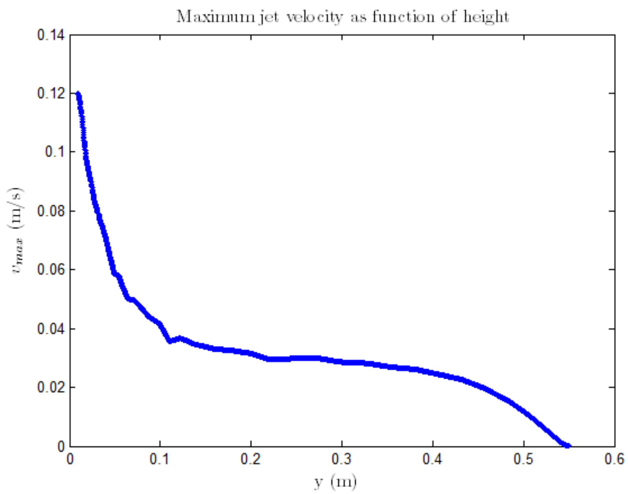

Figure 5.7: *Maximum value of v_y in the jet as a function of vertical distance from the actuator y.*

on the y-range that was experimentally investigated, limited by the extent of the laser sheet (approximately 100 mm in span). Within the latter range, the flux appears to increase linearly. At 100 mm distance from the actuator, it reaches a value of 0.0036 m^3s^{-1} per meter span, comparable in magnitude to the values seen in figure 4.4 and 4.7.

A maximum in $Q(y)$ is found at about $y = 0.3$ m, more or less at the horizontal centerline of the simulation's geometry, at a value of 0.011 m^3s^{-1} per meter span.

5.3 Validity of the model

Physically speaking, this model is not valid because it does not start from first principles and is based on certain unrealistic assumptions. For example, the charge density ρ_c between the electrodes remains unaffected by the external potential in the model and is also time-independent, meaning that the assumption is made that there is no movement of either positive or negative particles. However, it must be kept in mind that the purpose of the model is to keep computational time low by decoupling the electric field and the charge density.

The outcome of a simulation with this model depends on the value of a number of input parameters. Most of these were either taken from literature or taken identical to experimentally used parameters (see table F.1). An exception is the externally applied voltage. This voltage was chosen within the ranges typically found in literature (see chapter 2).

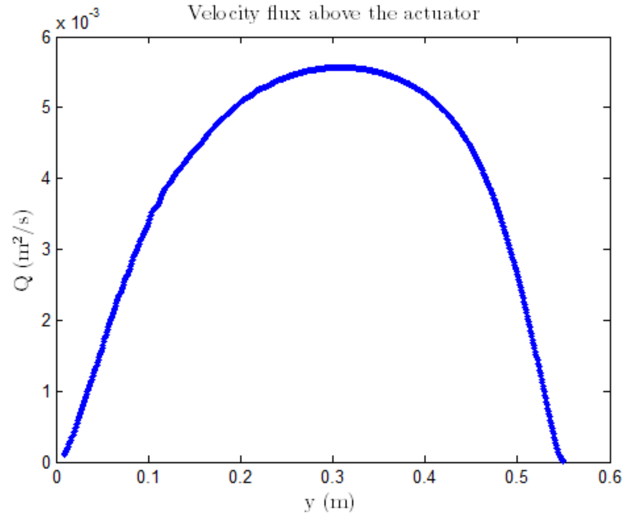

Figure 5.8: *2D velocity flux in the jet as a function of vertical distance from the actuator y, for the entire simulated y-range. The actuator surface starts at y = 0.01 m in the simulation.*

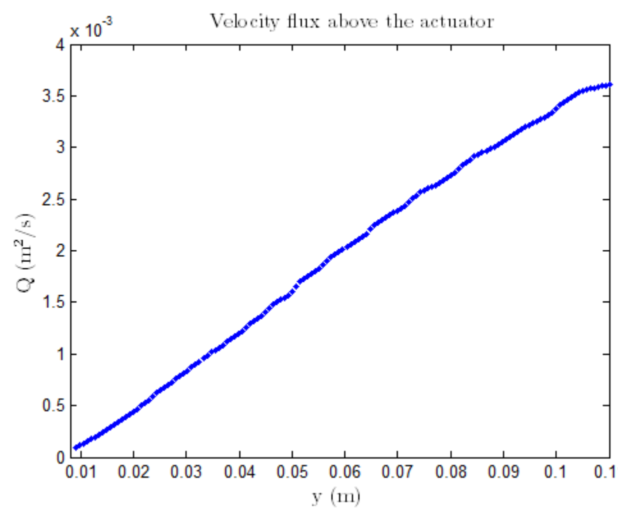

Figure 5.9: *2D velocity flux in the jet as a function of vertical distance from the actuator y, for the range as recorded during the experiments described in Chapter 4. The actuator surface starts at y = 0.01 m in the simulation.*

In this case, an applied voltage value of 12 kV was chosen to limit computational time before the simulation reached stability, which is almost 10 times the experimentally used average (absolute) value.

It must be noted here that, instead of tuning the applied voltage, a more physically valid method would have been to empirically obtain an order-of-magnitude indication of the charge density on the dielectric surface and implementing a value in this range as a boundary condition in the model. However, no measurements of this kind were performed, and for this reason the value of 0.0008 Cm^{-3} (from [37]) was kept fixed as the charge density on the lower electrode.

Nevertheless, with the 12 kV value, the model succeeds in producing an induced vertical jet with velocities in the same order of magnitude (0.1 ms^{-1}) as found experimentally. The development and order of magnitude of the velocity flux above the actuator $Q(y)$ also resemble the experimental results, which is important because this value can be used to estimate the net mass displacement by the actuator.

The main difference between the model and the experiments is that the jet in the model attains maximum velocity directly at the surface of the actuator and only decreases in strength with increasing y. This is in strong contrast to the experiments, in which the velocity was found (on average) to be maximal at a distance of 50 mm to 80 mm above the actuator.

To summarize, the model can be used to estimate the order of magnitude of induced jet velocities and of the velocity flux above the PSJA, keeping in mind that some input parameters may need to be chosen different from the experimentally used values. However, it does not succeed in replicating the general spatial structure of the jets.

Chapter 6

Conclusion and recommendations

This chapter summarizes the main findings and forwards recommendations for future research based on the conducted experiments.

6.1 Conclusion

The focus of this research was to experimentally determine the characteristics of the velocity profiles induced by a linear PSJA device in quiescent air at different pulsing frequencies and different duty cycles, using Particle Image Velocimetry (PIV).

In addition, a numerical simulation of PSJA operation has been performed, using approaches due to Suzen et al. [37] and Enloe et al. [17].

Two PSJA designs have been considered: one with non-adhesive copper strips glued to the dielectric (Duran glass), and one with adhesive copper tape of the same width and length. It was found that neither design could withstand a few tests without damage to the upper electrodes.

For this reason, the choice was made to perform the experimental study into pulsing frequency and duty cycle using the second actuator design and replacing the copper tape after each measurement, to ensure the best possible reproducibility of results with the available materials.

In the experiments, the pulsing frequency was varied between 30 Hz and 70 Hz (at 50% duty cycle) and the duty cycle between 20% and 65% (at 50 Hz pulsing frequency). It was found that the actuator performance - measured in terms of the maximum vertical velocity, the time-averaged maximum vertical velocity value as a function of distance from the actuator, and the time-averaged upwards velocity flux (velocity integrated over the horizontal actuator span) above the actuator - showed no significant dependence on both pulsing frequency and duty cycle.

The fact that no dependence on pulsing frequency was found is in contrast to earlier findings by Santhanakrishnan et al. [30]. The fact that no dependence on duty cycle was found is supported by results from Huang et al. [13]. The latter could have important consequences for industrial applications of PSJAs, because a large amount of energy can be saved by operating the devices at short duty cycles.

The maximum vertical velocities induced by PSJA operation all lay in the range between 0.11 ms^{-1} and 0.25 ms^{-1}, including standard deviations. These maximum values occurred at a distance between 50 mm and 80 mm above the actuator surface in almost every case. The maximum values for the velocity flux are all in the range 0.003 $\mathrm{m}^3\mathrm{s}^{-1}$ to 0.007 $\mathrm{m}^3\mathrm{s}^{-1}$ per meter span, and occurred at a distance between 50 mm and 90 mm above the actuator surface in almost every case.

The numerical method has been implemented in COMSOL 4.2a. For certain choices of parameters, it was able to replicate the order of magnitude of the velocity in the induced jet and of the velocity flux; however, it did not succeed in reproducing the spatial structure of the jets.

6.2 Recommendations

Another study, currently being conducted in this group, will focus on investigating the performance of a PSJA as a load control device on an airfoil in a subsonic wind tunnel, using the same PIV visualization and analysis techniques used here.

While no dependence on pulsing frequency and duty cycle was found, the structure and spread of the jets (as seen in Appendix E) was still found to differ for the various measurements. This might in part be down to experimental errors such as attaching the adhesive electrode tape wrongly, but further investigation into this matter is needed to determine what causes this unsteadiness.

One possibility is that the amount of analyzed frames per measurement was too low for a reliable analysis. The reason why, out of 1000 recorded frames, only 100 were taken for analysis is the high amount of required computational time (the processing of 1000 frames in PIVlab 1.31 took more than 18 hours on average). By using 100 frames, computational time was reduced by a large amount; however, this approach made the averaging less reliable, because not all structures in the flow field had characteristic time scales of less than 1.67 seconds. This might at least partly explain the differences between the time-averaged jets in Appendix E.

Another notable point is that the flow fields, which were assumed to be 2-dimensional because of the actuator symmetry, might in reality have contained significant 3-dimensional structures. A way of investigating this would be to shift the position of the laser sheet along the longitudinal axis of an actuator, and record the jet characteristics for different positions on the actuator.

The fact that the actuators used in this study were not durable without replacement of the upper electrodes is a reason for further investigations. If practical applications of PSJA devices are ever to be realized, research into the cause of the damage is necessary and durable designs for upper electrodes attached to a dielectric must be found.

Next to these practical matters, the theoretical background of plasma actuation is still not completely understood. Mainly the transfer of momentum from moving charged particles to the surrounding air is not clear. A better understanding of the exact processes taking place could lead to better optimization of plasma actuation, both for SDBD and PSJA devices.

Bibliography

[1] R. Foest, M. Schmidt, and K. Becker. Microplasmas, an emerging field of low-temperature plasma science and technology. *International Journal of Mass Spectrometry*, 248(3):87 – 102, 2006.

[2] John D. Anderson. *Fundamentals of Aerodynamics*. McGraw-Hill, New York, 2010.

[3] M. J. Druyvesteyn and F. M. Penning. The mechanism of electrical discharges in gases of low pressure. *Rev. Mod. Phys.*, 12:87–174, April 1940.

[4] Erik Wagenaars. *Plasma Breakdown of Low-Pressure Gas Discharges*. PhD Thesis. Technische Universiteit Eindhoven, Eindhoven, 2006.

[5] H. Raether. The electron avalanche and its development. *Applied Scientific Research, Section B*, 5:23–33, 1956. 10.1007/BF02933256.

[6] E. Kuffel, W.S. Zaengl, and J. Kuffel. *High Voltage Engineering Fundamentals*. Butterworth-Heinemann, Oxford, 2000.

[7] Yuri P. Raizer. *Gas Discharge Physics*. Springer-Verlag, 1991.

[8] Kogelschatz, U., Eliasson, B., and Egli, W. Dielectric-barrier discharges. principle and applications. *J. Phys. IV France*, 07:C4–47–C4–66, 1997.

[9] Enloe, C., Corke, T., Jumper, E., Kachner, K., McLaughlin, T., and Van Dyken, R. Mechanisms and responses of a single dielectric barrier plasma actuator: Plasma morphology. *AIAA Journal*, 42(3):589–594, March 2004.

[10] Dmitriy M. Orlov. *Modelling and Simulation of Single Dielectric Barrier Discharge Plasma Actuators*. University of Notre Dame, Indiana, 2006.

[11] M. Forte, J. Jolibois, J. Pons, E. Moreau, G. Touchard, and M. Cazalens. Optimization of a dielectric barrier discharge actuator by stationary and non-stationary measurements of the induced flow velocity: application to airflow control. *Experiments in Fluids*, 43:917–928, 2007. doi:10.1007/s00348-007-0362-7.

[12] Thomas, F., Corke, T., Iqbal, M., Kozlov, K., and Schatzman, D. Optimization of dielectric barrier discharge plasma actuators for active aerodynamic flow control. *AIAA Journal*, 47(9):2169–2178, September 2009.

[13] Junhui Huang, Thomas C. Corke, and Flint O. Thomas. Unsteady plasma actuators for separation control of low-pressure turbine blades. *AIAA Journal*, 44:1477–1487, 2006.

[14] Corke, Thomas C., Post, Martiqua L., and Orlov, Dmitriy M. Single dielectric barrier discharge plasma enhanced aerodynamics: physics, modeling and applications. *Experiments in Fluids*, 46:1–26, 2009.

[15] J. Pons, E. Moreau, and G. Touchard. Asymmetric surface dielectric barrier discharge in air at atmospheric pressure: electrical properties and induced airflow characteristics. *Journal of Physics D: Applied Physics*, 38(19):3635, 2005.

[16] Alexandre V. Likhanskii, Mikhail N. Shneider, Sergey O. Macheret, and Richard B. Miles. Modeling of dielectric barrier discharge plasma actuator in air. *J. Appl. Phys.*, 103(053305), 2008.

[17] Enloe, C., McLaughlin, T., Van Dyken, R., Kachner, K., Jumper, E., Corke, T., Post, M., and Haddad, O. Mechanisms and responses of a single dielectric barrier plasma actuator: Geometric effects. *AIAA Journal*, 42(3):595–604, March 2004.

[18] N. Balcon, N. Benard, Y. Lagmich, J.-P. Boeuf, G. Touchard, and E. Moreau. Positive and negative sawtooth signals applied to a DBD plasma actuator - influence on the electric wind. *Journal of Electrostatics*, 67(23):140 – 145, 2009.

[19] M. Kotsonis and S. Ghaemi. Forcing mechanisms of dielectric barrier discharge plasma actuators at carrier frequency of 625 Hz. *J. Appl. Phys.*, 110(11), 2011.

[20] Martiqua L. Post. *Plasma actuators for separation control on Stationary and Oscillating Airfoils*. University of Notre Dame, Indiana, 2004.

[21] Jesse Little, Keisuke Takashima, Munetake Nishihara, Igor Adamovich, and Mo Samimy. Separation control with nanosecond-pulse-driven dielectric barrier discharge plasma actuators. *AIAA Journal*, 50(2):350–365, February 2012.

[22] Michael Amitay and Ari Glezer. Aerodynamic flow control using synthetic jet actuators. In *Control of Fluid Flow*, volume 330 of *Lecture Notes in Control and Information Sciences*, pages 45–73. Springer Berlin / Heidelberg, 2006. 10.1007/978-3-540-36085-82.

[23] R. Duvigneau, A. Hay, and M. Visonneau . Optimal location of a synthetic jet on an airfoil for stall control. *J. Fluids Eng.*, 129(7):825, 2007.

[24] James Whitehead and Ismet Gursul. Interaction of synthetic jet propulsion with airfoil aerodynamics at low Reynolds numbers. *AIAA Journal*, 44(8):1753–1766, August 2006.

[25] Barton L. Smith and Ari Glezer. The formation and evolution of synthetic jets. *Phys. Fluids*, 10(9):2281–2297, 1998.

[26] M. Ciuryla, Y. Liu, J. Farnsworth, C. Kwan, and M. Amitay. Flight control using synthetic jets on a Cessna 182 model. *J. Aircr.*, 44(2):642–653, 2007.

[27] Shan Zhong, Mark Jabbal, Hui Tang, Luis Garcillan, Fushui Guo, Norman Wood, and Clyde Warsop. Towards the design of synthetic-jet actuators for full-scale flight conditions, part I. *Flow, Turbulence and Combustion*, 78:283–307, 2007. 10.1007/s10494-006-9064-0.

[28] Hui Tang, Shan Zhong, Mark Jabbal, Luis Garcillan, Fushui Guo, Norman Wood, and Clyde Warsop. Towards the design of synthetic-jet actuators for full-scale flight conditions, part II. *Flow, Turbulence and Combustion*, 78:309–329, 2007. 10.1007/s10494-006-9061-3.

[29] Jamey D. Jacob, Karthik Ramakumar, Rich Anthony, and Richard B. Rivir. Control of laminar and turbulent shear flows using plasma actuators. 2005. 4th International Symposium on Turbulence and Shear Flow Phenomena.

[30] Arvind Santhanakrishnan and Jamey D. Jacob. Flow control with plasma synthetic jet actuators. *Journal of Physics D: Applied Physics*, 40(3):637–651, 2007.

[31] Arvind Santhanakrishnan, Daniel A. Reasor, and Raymond P. LeBeau. Characterization of linear plasma synthetic jet actuators in an initially quiescent medium. *Phys. Fluids*, 21(043602), 2009.

[32] Arvind Santhanakrishnan, Jamey D. Jacob, and Yildirim B. Suzen. Flow control using plasma actuators and linear/annular plasma synthetic jet actuators. Paper No. 2006-3033, 3rd AIAA Flow Control Conference, June 58, San Francisco, CA.

[33] Michael Bolitho and Jamey D. Jacob. Thrust vectoring flow control using plasma synthetic jet actuators. 46th AIAA Aerospace Sciences Meeting and Exhibit 7 - 10 January 2008, Reno, Nevada.

[34] J. P. Boeuf and L. C. Pitchford. Electrohydrodynamic force and aerodynamic flow acceleration in surface dielectric barrier discharge. *Phys. Fluids*, 97(103307), 2005.

[35] Balaji Jayaraman, Young-Chang Cho, and Wei Shyy. Modeling of dielectric barrier discharge plasma actuator. 38th AIAA Plasmadynamics and Lasers Conference, 25 - 28 June 2007, Miami, FL.

[36] Hiroyuki Nishida, Taku Nonomura, and Takashi Abe. Numerical analysis on three-dimensional body force field of DBD plasma actuator. 43rd AIAA Plasmadynamics and Lasers Conference, 25 - 28 June 2012, New Orleans, Louisiana.

[37] Y. B. Suzen, P. G. Huang, J. D. Jacob, and D. E. Ashpis. Numerical simulations of plasma based flow control applications. 35th Fluid Dynamics Conference and Exhibit June 6-9, 2005, Toronto, Ontario.

[38] W. Shyy, B. Jayaraman, and A. Andersson. Modeling of glow discharge-induced fluid dynamics. *J. Appl. Phys.*, 92(11):6434–6443, December 2002.

[39] A. B. Liu, P. F. Zhang, B. Yan, C. F. Dai, and J. J. Wang. Flow characteristics of synthetic jet induced by plasma actuator. *AIAA Journal*, 49(3):544–553, March 2011.

[40] Thomas C. Corke, C. Lon Enloe, and Stephen P. Wilkinson. Dielectric barrier discharge plasma actuators for flow control. *Annual Review of Fluid Mechanics*, 42:505–529, 2010.

Appendix A

Pictures of the experimental setup

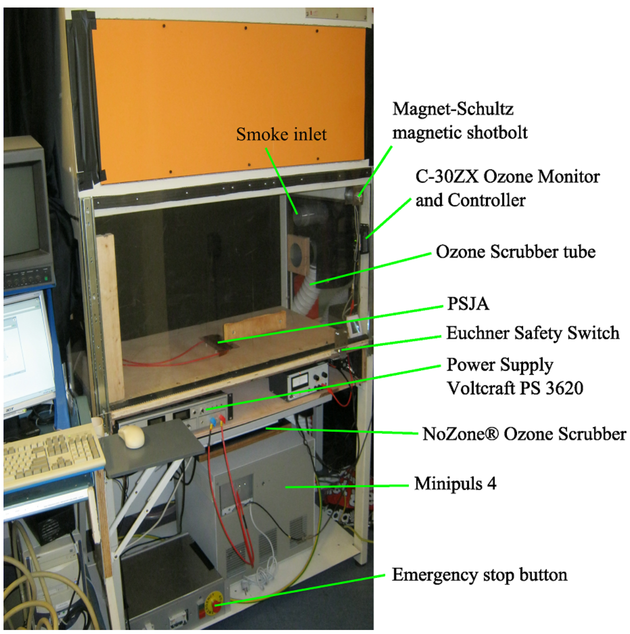

Figure A.1: *The main hardware of the setup as described in Chapter 3.*

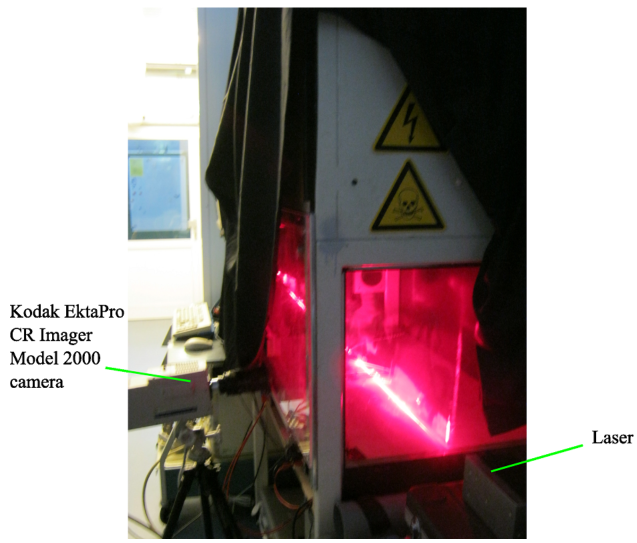

Figure A.2: *The parts for PIV measurements*

Figure A.3: *The laser sheet above a (non-operating) PSJA*

Appendix B

Choice of parameters

In this study, the behavior of the PSJA was investigated as a function of pulsing frequency and duty cycle. The aim was to operate the PSJA with a pulsed sinusoidal waveform. In order to ensure that the input voltage for the PSJA was as desired, the voltage output of the Minipuls 4 had to be measured directly.

The Minipuls 4 is able to transform a square input waveform into a sinusoidal waveform, due to the TTL logic at the control input. Therefore, the LABview-generated waveforms were set to be square-wave pulse trains, so that the Minipuls 4 output would be sine-shaped pulse trains. One period of the used LABview waveforms, between $t = 0$ and $t = 1/f_{pulse}$, is given by the general formula

$$f(t) = \begin{cases} A + B\,\mathrm{sgn}\left(\sin[2\pi f_{drive} t]\right) & : t < d/f_{pulse} \\ C & : t > d/f_{pulse} \end{cases}$$

where A is the square wave offset (V), B is the amplitude of the square waves (V), f_{drive} is the frequency of the square waves (Hz), f_{pulse} is the frequency of the pulse trains (Hz), d is the duty cycle fraction ($0 < d < 1$) and C is the voltage during the passive phase of the duty cycle (V).

B.1 Pulse frequency

Measurements were conducted in the range of pulse frequencies between 10 and 100 Hz (a range also studied in part by Santhanakrishnan et al. [30]) to determine whether the Minipuls 4 output was adequate in all cases. The constant settings for the LABview-generated square waveforms were a 50% duty cycle (d=0.5), a voltage amplitude of $B = 1.0$ V during the active phase of the duty cycle, an offset of $A = 1.0$ V and an f_{drive} of 13 kHz. The voltage during the passive phase of the duty cycle was set

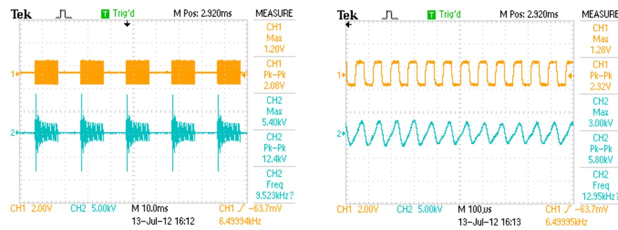

Figure B.1: *The LABview output (channel 1) and the Minipuls 4 output (channel 2) as recorded by the oscilloscope. The right recording is a close-up of the pulse packages in the left one. The pulsing frequency was 50 Hz.*

to $C = 1.0$ V; this resulted in a zero voltage at the Minipuls 4 output due to the TTL logic. The DC voltage generated by the Power Supply Voltcraft PS 3620 was kept constant at 10.5 V.

For f_{pulse} values below 20 Hz, the current drawn by the Minipuls 4 exceeded the limit allowed by the Power Supply Voltcraft PS 3620, so these frequencies were not used.

For higher values of f_{pulse}, the induced output waveforms were found to be sinusoidal pulse trains, as required; however, their amplitude was found to decrease during the active part of the duty cycle. See figure B.1, which depicts the LABview output (channel 1) and Minipuls 4 output (channel 2) as recorded by the oscilloscope, at a pulsing frequency of 50 Hz, on two time scales. It can be seen that the peak-to-peak voltage of the LABview output was not exactly 2 V as set beforehand; but this was not considered a problem as long as it remained constant.

For pulse frequencies above 80 Hz, the waveforms were seen to lose their sinusoidal shape and get heavily distorted in the middle. See figure B.2. For this reason, pulse frequencies above 80 Hz were not used.

In order to validate the Minipuls output in the pulse frequency range between 30 Hz and 70 Hz, the results of the measurements were post-processed

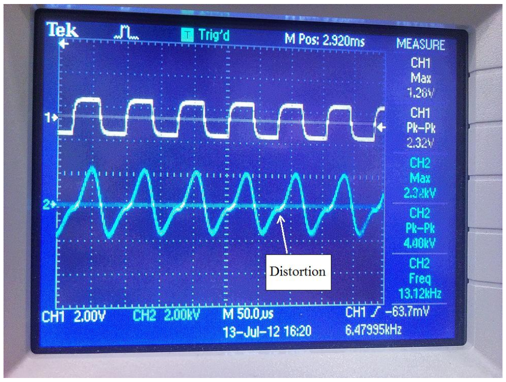

Figure B.2: *Distortion in the sine shape at* f_{pulse}*=80 Hz*

with Matlab to perform a Fourier analysis on the signals from the oscilloscope. In all cases, the main frequency component of both channels was found to be equal, at 13 kHz, as desired. See figure B.3 for an example of the Fourier series of both channels, at a pulsing frequency of 70 Hz.

In order to check that the Minipuls 4 output did not change its characteristics over the range of pulse frequencies, the maximum and average absolute amplitude of the active parts of the cycle were recorded as a function of pulsing frequency. See figure B.4.

While the narrow peaks observed at the beginning of each duty cycle were seen to differ in amplitude, the average amplitude during the active part was approximately the same for each pulsing frequency. This amplitude is in the range 1.58 kV $\pm$ 0.06 kV. Coupled with the fact that, for pulse frequencies between 30 Hz and 70 Hz, the driving frequency and duty cycle were exactly as desired and the sinusoidal waveform did not exhibit heavy distortions, this range was considered to be appropriate for conducting measurements on PSJA behavior as a function of pulse frequency of sinusoidal wave trains.

B.2 Duty cycle

A similar analysis has been perfomed for variations of the duty cycle at a pulsing frequency of 50 Hz. The other constant settings for the LABview-generated square waveforms were a voltage amplitude of 1.0 V during the active phase, a constant voltage of 1.0 V during the passive phase, and a driving frequency of 13 kHz, as before.

For duty cycles of 10% or lower, the output waveform was found to consist almost solely of initial, high peaks and therefore not considered appropriate as part of a measurement program. For duty cycles higher than 70%, the peak value of the Minipuls 4 output voltage exceeded the maximum allowed value within safety limits (40 kV peak-to-peak), and therefore higher duty cycles were not used either.

As earlier, the driving frequency, pulse frequency and duty cycle of the Minipuls 4 output waveform were found to be exactly as desired; however, again, the amplitude was not constant. Plots of the maximum and average amplitude of the active parts of the output waveform as a function of duty cycle are given in figure B.5.

Here, it was found that both the maximum and the average absolute amplitude at the Minipuls 4 output decreased with duty cycle. The latter appears to be logical, given that the initial high peaks of each pulse package will constitute an ever smaller part of the active phase with increasing duty cycle.

The average absolute amplitude should remain constant over the range of duty cycles in order to be able to draw valid conclusions regarding the behavior of a PSJA as a function of duty cycle. The approach for realizing this was to calibrate the active-phase amplitude in LABview for a number of values of duty cycle in the range 20% to 65%, in such a way that the corresponding average absolute amplitudes at the Minipuls 4 output were (approximately) equal.

Measurements were performed to determine the required active-phase voltage values in LABview. For these measurements, the DC voltage generated by the Power Supply Voltcraft PS 3620 was kept constant at 11 V. The pulse frequency was kept at 50 Hz, in the middle of the earlier-found valid pulse frequency range. The results are given in table B.1. A plot displaying the corresponding maximum and average absolute amplitudes at the Minipuls 4 output is given in figure B.6. The latter values lay within the range 1.4 kV $\pm$ 0.075 kV.

The values in table B.1 were used as active-phase LABview voltage values during the duty cycle measurements, the results of which can be found in chapter 4. For duty cycle values inbetween those given in the table, the voltage values were interpolated.

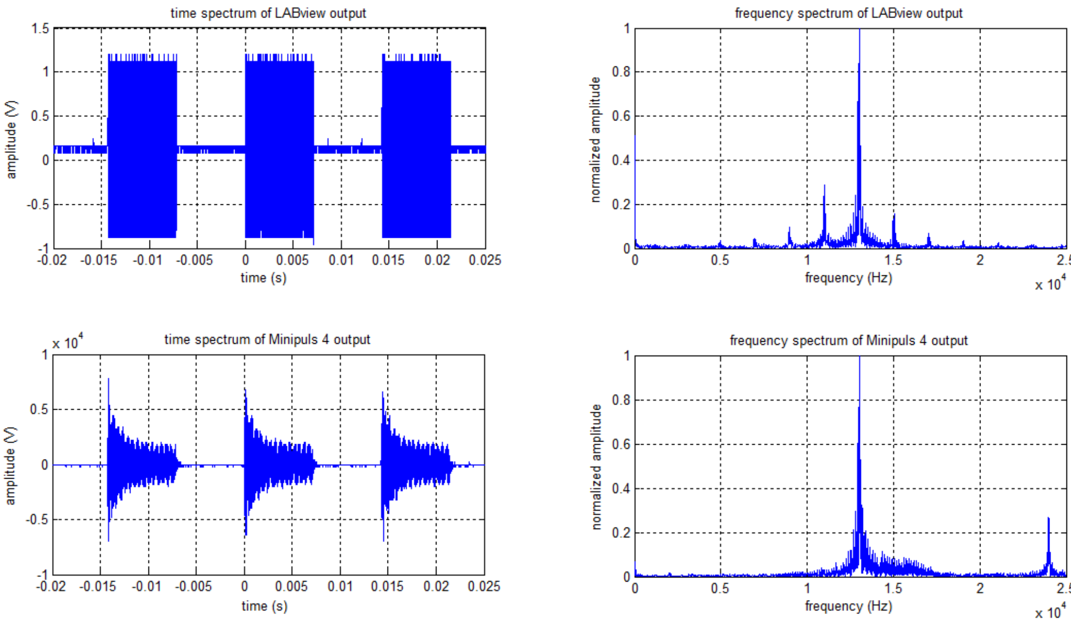

Figure B.3: *Time and frequency domains of the LABview and Minipuls 4 output, at a pulsing frequency of 70 Hz. The main frequency component is exactly 13 kHz in both cases.*

Table B.1: *Voltage amplitude values in LABview as used during duty cycle measurements*

Duty cycle	LABview amplitude
20 %	2.0 V
30 %	1.3 V
40 %	1.2 V
50 %	1.1 V
60 %	1.0 V
65 %	1.0 V

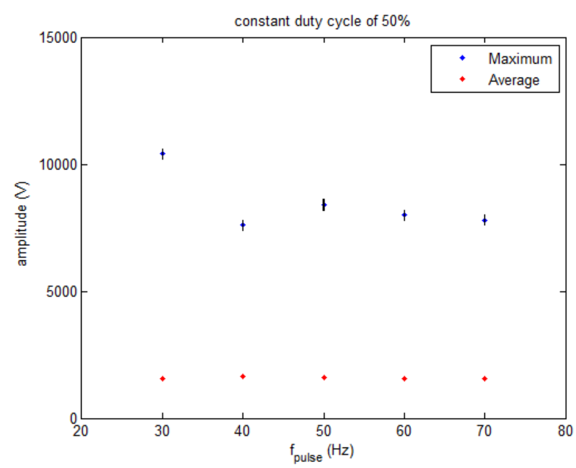

Figure B.4: *Maximum and averaged absolute amplitude of Minipuls 4 output as a function of f_{pulse}. The error bars in the maximum series (±200 V) are taken from the fluctuations in recorded output during the passive part of the duty cycle.*

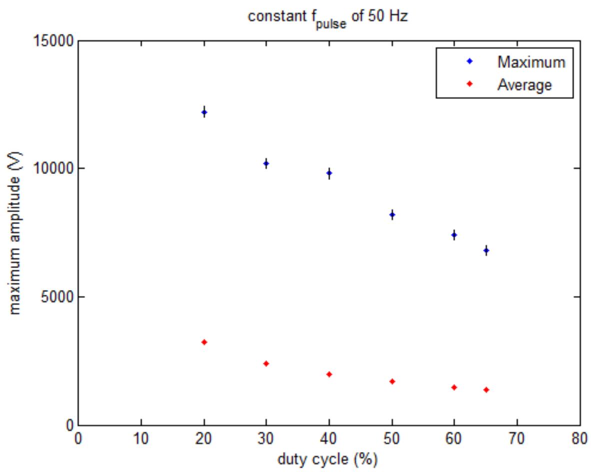

Figure B.5: *Maximum and averaged absolute amplitude of Minipuls 4 output as a function of duty cycle. The error bars in the maximum series (±200 V) are taken from the fluctuations in recorded output during the passive part of the duty cycle.*

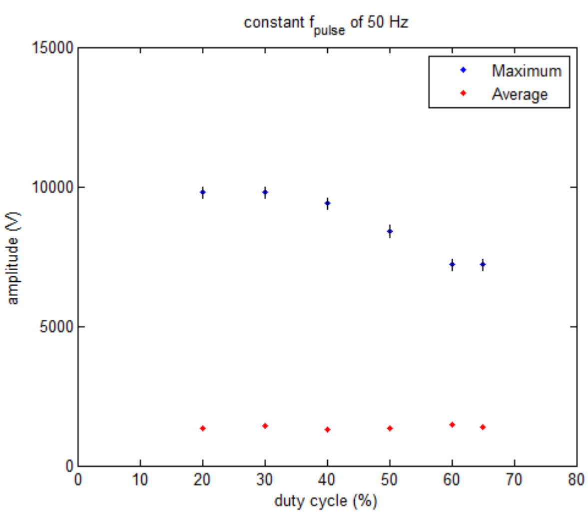

Figure B.6: *Maximum and averaged absolute amplitude of Minipuls 4 output as a function of duty cycle, using adapted amplitudes in LABview for every duty cycle (see table B.1). The error bars in the maximum series (±200 V) are taken from the fluctuations in recorded output during the passive part of the duty cycle.*

Appendix C

PSJA durability tests

The durability of the two actuators with non-adhesive copper strips and the actuator with Advance adhesive copper tape was examined by supplying them with pulse trains for 40 seconds at a time. This waveform was applied at ~30-minute intervals.

During all tests, the PSJA input waveform had a pulsing frequency of 30 Hz and a driving frequency of 13 kHz. The voltage from the Power Supply Voltcraft was kept at 11.2 V. The first and third actuator were tested 5 times at 50% duty cycle, the second one was tested 5 times at 20% duty cycle. The LABview amplitude calibration as described in Appendix B was applied to keep the Minipuls 4 average absolute output amplitude constant.

For all three actuators, PIV measurements of the induced flow field above the actuator were taken during the first, third and fifth test. Analysis of 100 of the recorded frames was performed with PIVlab 1.31.

First actuator (non-adhesive copper strips)

Figure C.1 shows the average value of the maximum velocity from each pair of frames, here called $\overline{v_{max}}$, for the first actuator. The error bars in the plot represent the standard deviation of the maximum velocities.

The vertical velocity distribution was also averaged over all 99 pairs of frames. The time-averaged velocity plots for all three recordings are given in figure C.2. The velocity profiles in the second and third recording much less resemble a stable jet than during the first test.

Figure C.3 shows the maximum vertical velocity in this average distribution, called $\overline{v}_{max}(y)$, as a function of distance from the actuator surface for each recorded test.

From this analysis, it can be seen that both $\overline{v_{max}}$ and $\overline{v}_{max}(y)$ decreased after the first measurement. In the first test, the found value for $\overline{v_{max}}$ was 0.159 ms^{-1} $\pm$ 0.039 ms^{-1}. After only two operations, this value had almost halved, to 0.089 ms^{-1} $\pm$ 0.011 ms^{-1}.

By the time of the third operation, the induced discharges had started to look heavily asymmetrical and inhomogeneous across the two electrodes. The jet at times resembled an SDBD discharge (tangential to the actuator surface), indicating a very uneven degeneration of the electrodes.

Second actuator (non-adhesive copper strips)

The results for the second actuator, tested at 20% duty, can be found in figures C.4, C.5 and C.6.

Just as for the first actuator, $\overline{v_{max}}$ and $\overline{v}_{max}(y)$ decreased as the number of conducted tests increased. This actuator seemed to degenerate slightly less quickly than the first one; nevertheless, the value found for $\overline{v_{max}}$ decreased from 0.144 ms^{-1} $\pm$ 0.014 ms^{-1} to 0.083 ms^{-1} $\pm$ 0.010 ms^{-1} within five tests, and the average velocity distribution of the fifth test bore little resemblance to the jet from the first test.

Third actuator (Adhesive copper tape)

The results for the test on the actuator design with Advance adhesive copper tape as upper electrodes are given in figure C.7, C.8 and C.9.

This actuator clearly lasted longer than those with non-adhesive copper strips as upper electrode material in terms of the maximum induced velocity and the structure of the vertical velocity distribution. However, the light emitted during the discharges was seen to decrease in intensity as more tests were conducted on the actuator, indicating that this design, too, is not durable for more than 5 operations.

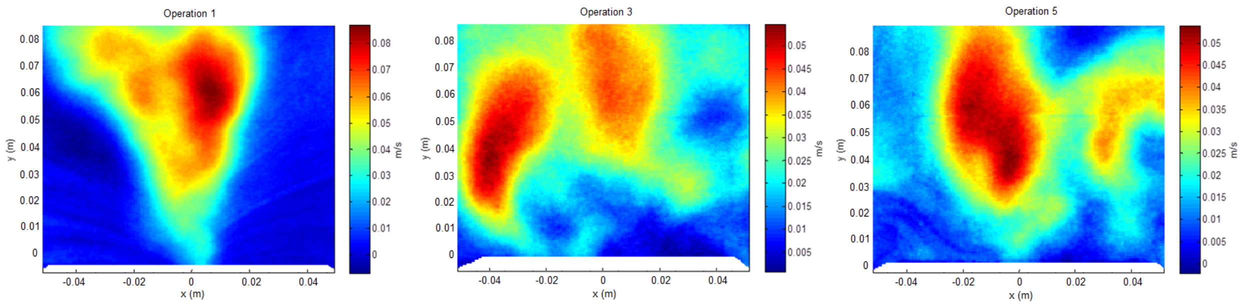

Figure C.2: *The time-averaged vertical velocity distributions for the actuator tested at 50% duty cycle, for tests no. 1 (left), 3 (middle) and 5 (right).*

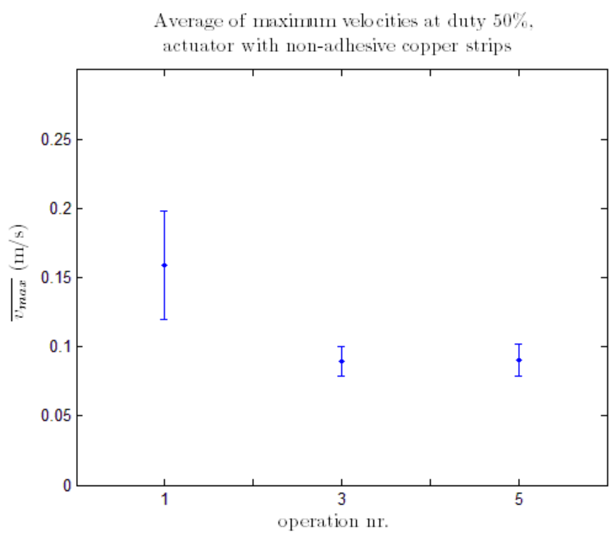

Figure C.1: $\overline{v_{max}}$ *versus the number of the conducted test, for the actuator tested at 50% duty cycle.*

Conclusion

From these durability tests, two conclusions can be drawn. Firstly, it can be stated that the performance of an actuator with the used kind of non-adhesive copper strips shows a significant decrease of $\overline{v_{max}}$ as function of the number of tests conducted with it. It can also be noted that this decreasing performance is stronger for a 50 % duty cycle than a 20 % duty cycle.

The durability of these actuators with non-adhesive copper strips is clearly too low to use them for a study regarding electrical parameters such as pulsing frequency and duty cycle. The measurements would not be reproducible. A possible recommendation to examine the behaviour of this kind of PSJA as a function of such parameters in a valid way would be to use a new actuator for each measurement.

For an as yet unknown reason, the actuator design with Advance adhesive copper tape was able to withstand more tests than the actuators with non-adhesive copper strips.

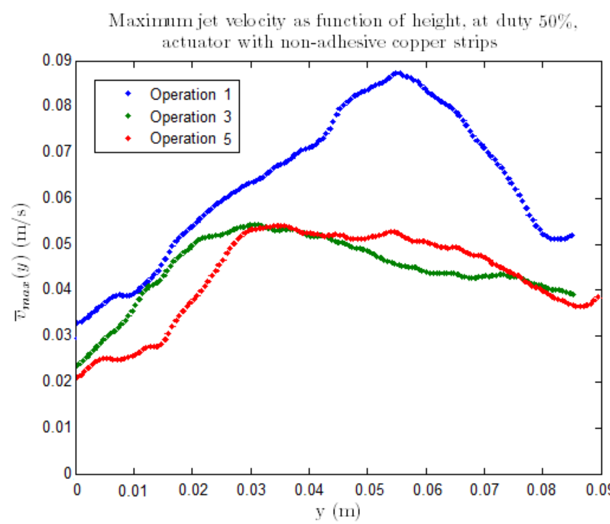

Figure C.3: $\overline{v}_{max}(y)$ *for all three tests conducted at 50% duty cycle. The actuator surface is situated at $y = \sim 0$ m.*

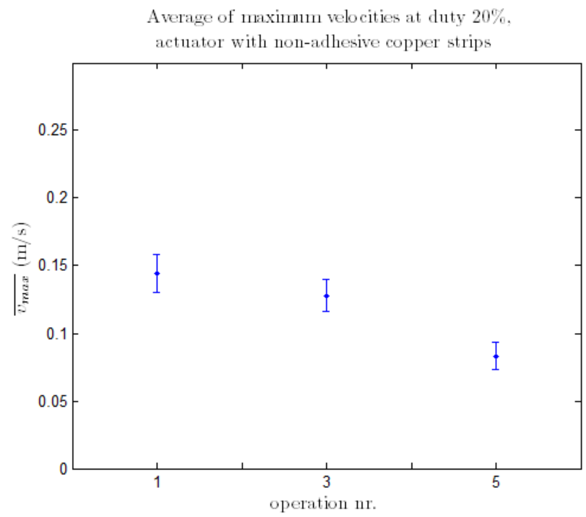

Figure C.4: *$\overline{v_{max}}$ versus the number of the conducted test, for the actuator tested at 20% duty cycle.*

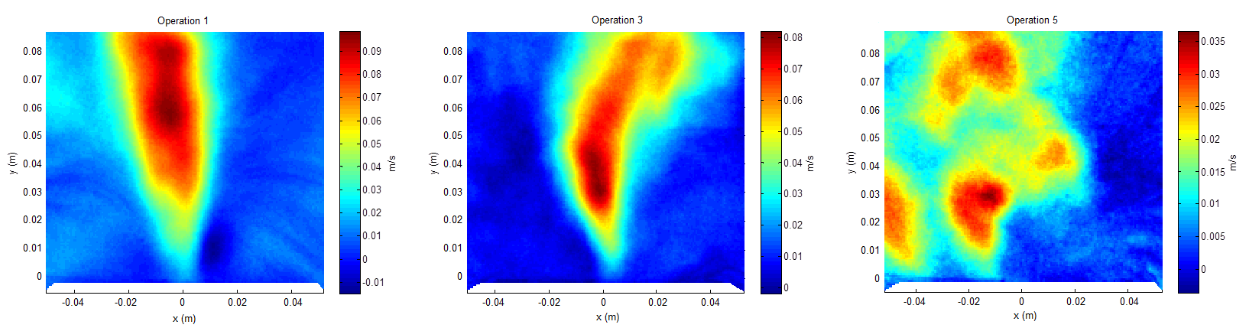

Figure C.5: *The time-averaged vertical velocity distributions for the actuator tested at 20% duty cycle, for tests no. 1 (left), 3 (middle) and 5 (right).*

Figure C.6: *$\overline{v}_{max}(y)$ for all three tests conducted at 20% duty cycle. The actuator surface is situated at $y = \sim 0$ m.*

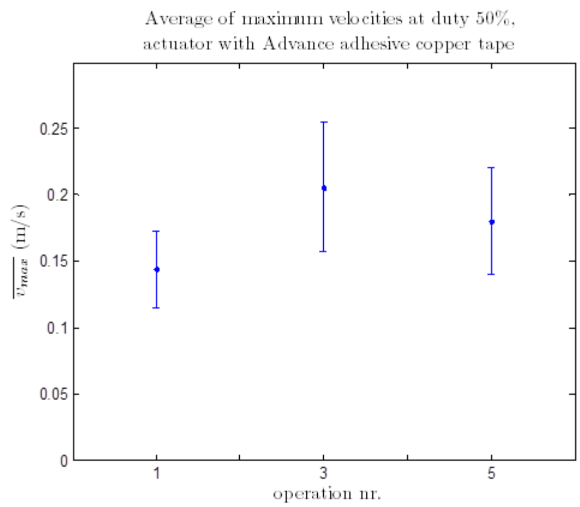

Figure C.7: $\overline{v_{max}}$ *versus the number of the conducted test, for the actuator design with Advance adhesive copper tape.*

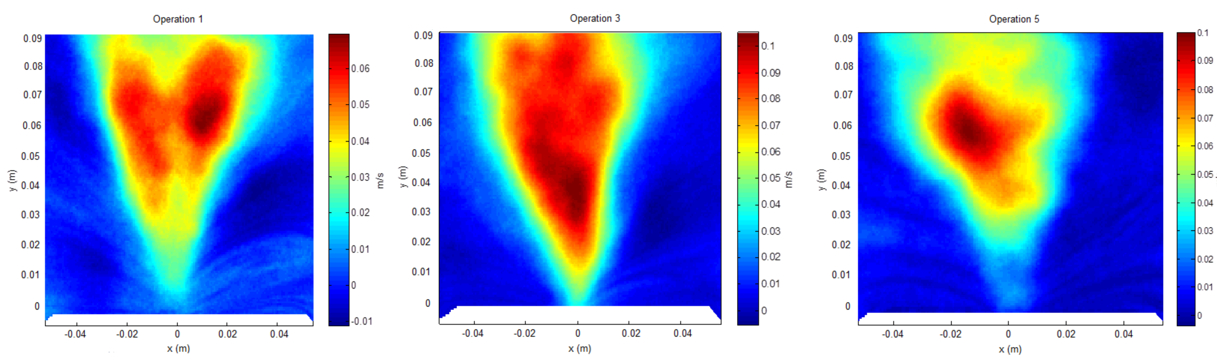

Figure C.8: *The time-averaged vertical velocity distributions for the actuator design with Advance adhesive copper tape, for tests no. 1 (left), 3 (middle) and 5 (right).*

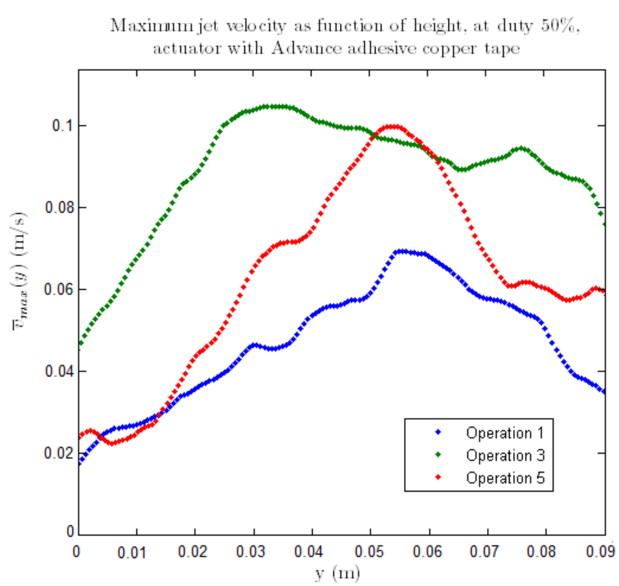

Figure C.9: $\overline{v}_{max}(y)$ *for all three tests conducted with the actuator design with Advance adhesive copper tape. The actuator surface is situated at* $y = \sim 0$ *m.*

Appendix D

Experimental protocol

This section details the way in which the measurement series regarding pulse frequency and duty cycle, as described in chapters 3 and 4, were performed.

Prior to measurements

Before each measurement series, a calibration for a reference distance in the to-be-recorded images was performed with a ruler, along the same line that the laser sheet would be positioned to follow during the measurements. The position of the camera and of the actuator was checked before each measurement, with the actuator in the middle of the cabinet and in good focus in the bottom middle of the camera image.

Measurements

For the PIV measurements themselves, the following protocol was carried out:

1. Fog was injected into the cabinet for a couple of seconds. Subsequently, the fog injection tube was closed off.
2. The laser was turned on and positioned perpendicularly to the actuator, along the same line on which the calibration with the ruler had been performed earlier.
3. The Power Supply Voltcraft was turned on. The voltage display was set to 11.2 V, which induced the brightest discharge.
4. $\sim$60 seconds were allowed to pass to allow the fog to settle uniformly within the cabinet.
5. The output of the Power Supply Voltcraft was turned on. Directly afterwards, the LABview function generator was run.
6. The camera recording (60 fps) was started. The total number of frames per recording was 2046, so at 60 fps one recording took 34.2 seconds.
7. When the recording was finished, the laser, LABview function generator, and Power Supply Voltcraft were shut off.
8. Frames nr. 1000 to 2000 of the recording, representing the induced velocity field when the actuator had already been on for 16.7 seconds, were saved as .tif files for the analysis.

Post-measurements

After each measurement, the following procedure was performed:

1. A waiting period of a few minutes was allowed to pass until the fog had disappeared from the cabinet.
2. The NoZone® Ozone Scrubber was turned on in case the ozone concentration had risen above 0.05 ppm.
3. The upper electrodes on the actuator were replaced by new ones.

Subsequently, the measurement protocol was repeated for a different value of pulsing frequency or duty cycle.

Analysis with PIVlab 1.31

For the analysis, the following procedure was followed:

1. For each investigated value of pulsing frequency or duty cycle, 100 frames were taken from the recording and imported in PIVlab 1.31.

Table D.1: *Interrogation area settings as used in the PIVlab 1.31 analysis of the recordings*

Pass	Area (px)	Step (px)
1	64	32
2	32	16
3	16	8
4	4	2

2. The Sequencing style was set to 1-2, 2-3, 3-4, …

3. A global ROI (Region of Interest) was selected to leave out the upper part of each recording, which the laser sheet was not wide enough to cover and which was therefore mostly black in the recording. See figure D.1.

4. A mask covering the actuator surface, present at the bottom of each recording, was applied to all frames to ensure that no reflections from the electrode tape were taken along in the PIV analysis. See figure D.1.

5. To improve the images' contrast, CLAHE was applied at a window size of 40 pixels.

6. "FFT window deformation" was selected as the PIV algorithm. Four interrogation areas were selected. See table D.1. As deformation interpolator, spline was selected. The sub-pixel estimator was set to Gauss 2x3-point. See also figure D.1.

7. The analysis was performed.

8. After completion, calibration regarding distance was performed with the calibration image of a ruler. The time step was entered as 17 ms.

9. A plot was made in PIVlab 1.31 of the velocity magnitude and missing values were computed through interpolation. Subsequently, the data for x, y, the horizontal velocity u and the vertical velocity v were exported in ASCII format.

10. The further processing of this data was straightforward, and was performed with MATLAB.

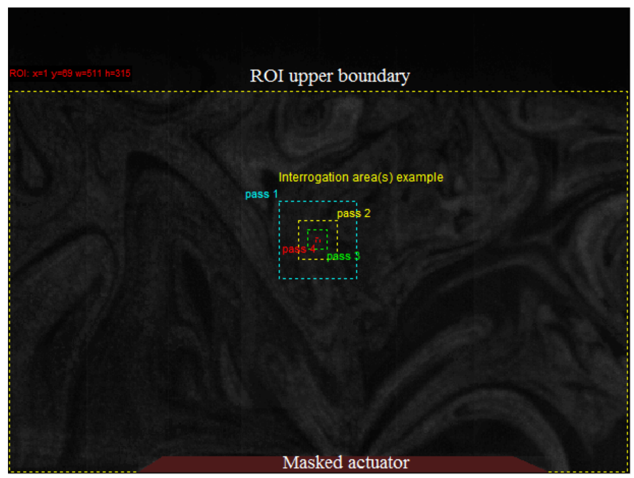

Figure D.1: *The ROI, mask, and interrogation areas displayed in a contrast-enhanced frame from the PIV experiments, taken at 40% duty cycle in the duty cycle series.*

Appendix E

Pictures from PIV analysis

This section displays the time-averaged (1.67 seconds) distributions of the vertical velocity above the actuator as found for every investigated pulsing frequency and duty cycle. Note that the maximum velocities in these pictures do *not* correspond to the maximum velocities found in figures 4.2 and 4.5. Those plots show the *time-averaged value of the spatial maximum velocities*, whereas the pictures in this section show the *time-averaged velocity distribution and the spatial maximum value herein.*

Pulsing frequency series (50% duty)

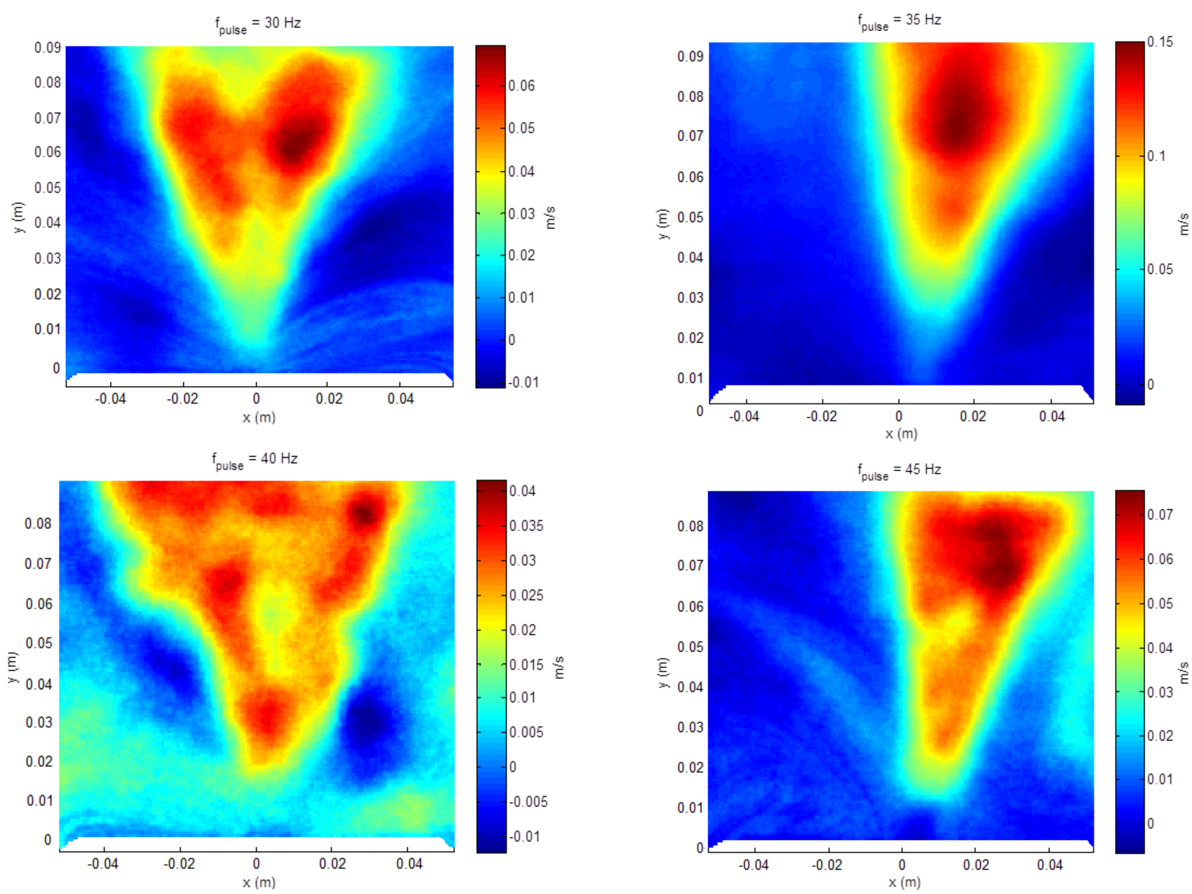

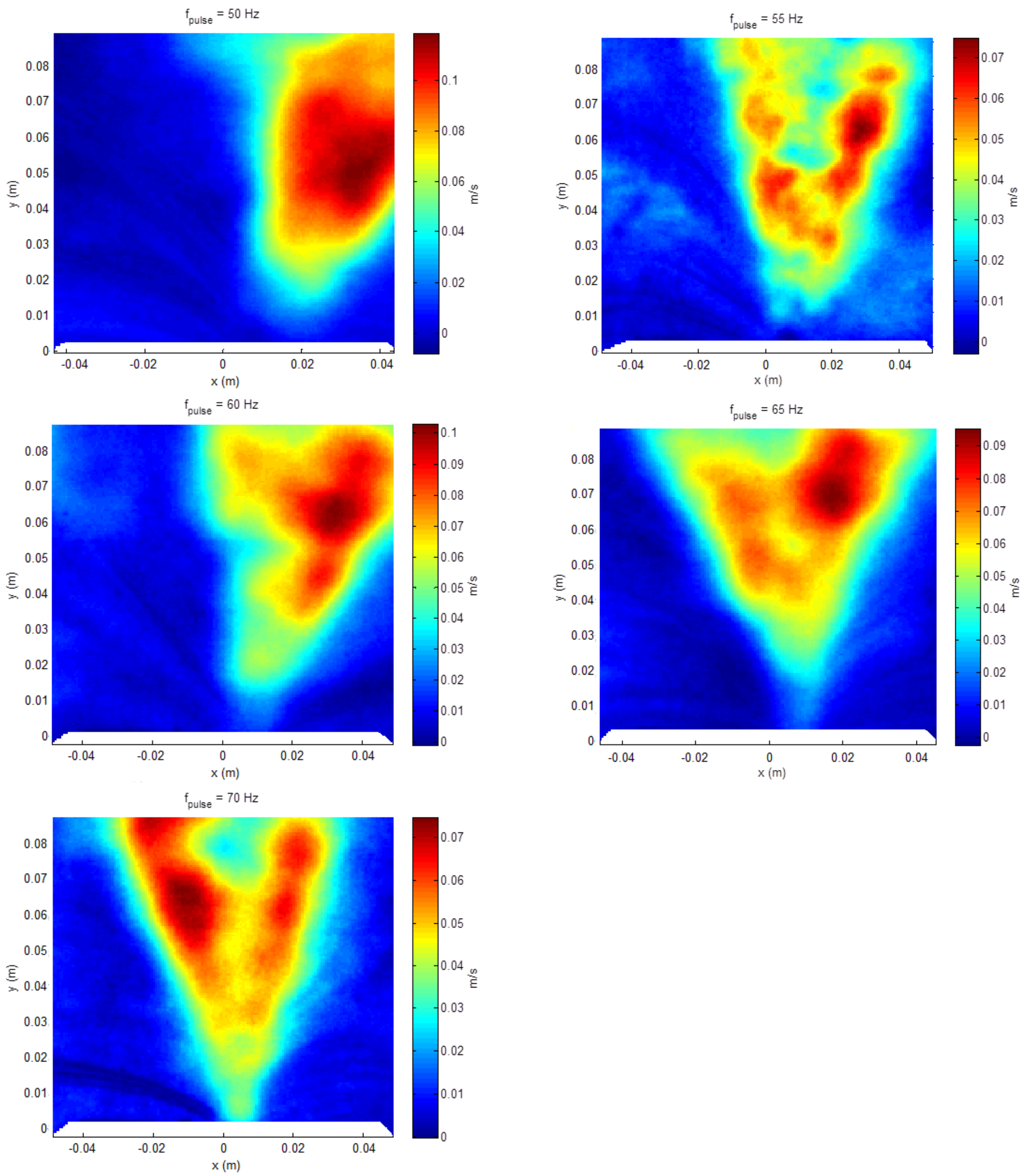
fpulse = 50 Hz
y (m)
x (m)
m/s
fpulse = 55 Hz
y (m)
x (m)
m/s
fpulse = 60 Hz
y (m)
x (m)
m/s
fpulse = 65 Hz
y (m)
x (m)
m/s
fpulse = 70 Hz
y (m)
x (m)
m/s

Duty cycle series (f_{pulse} = 50 Hz)

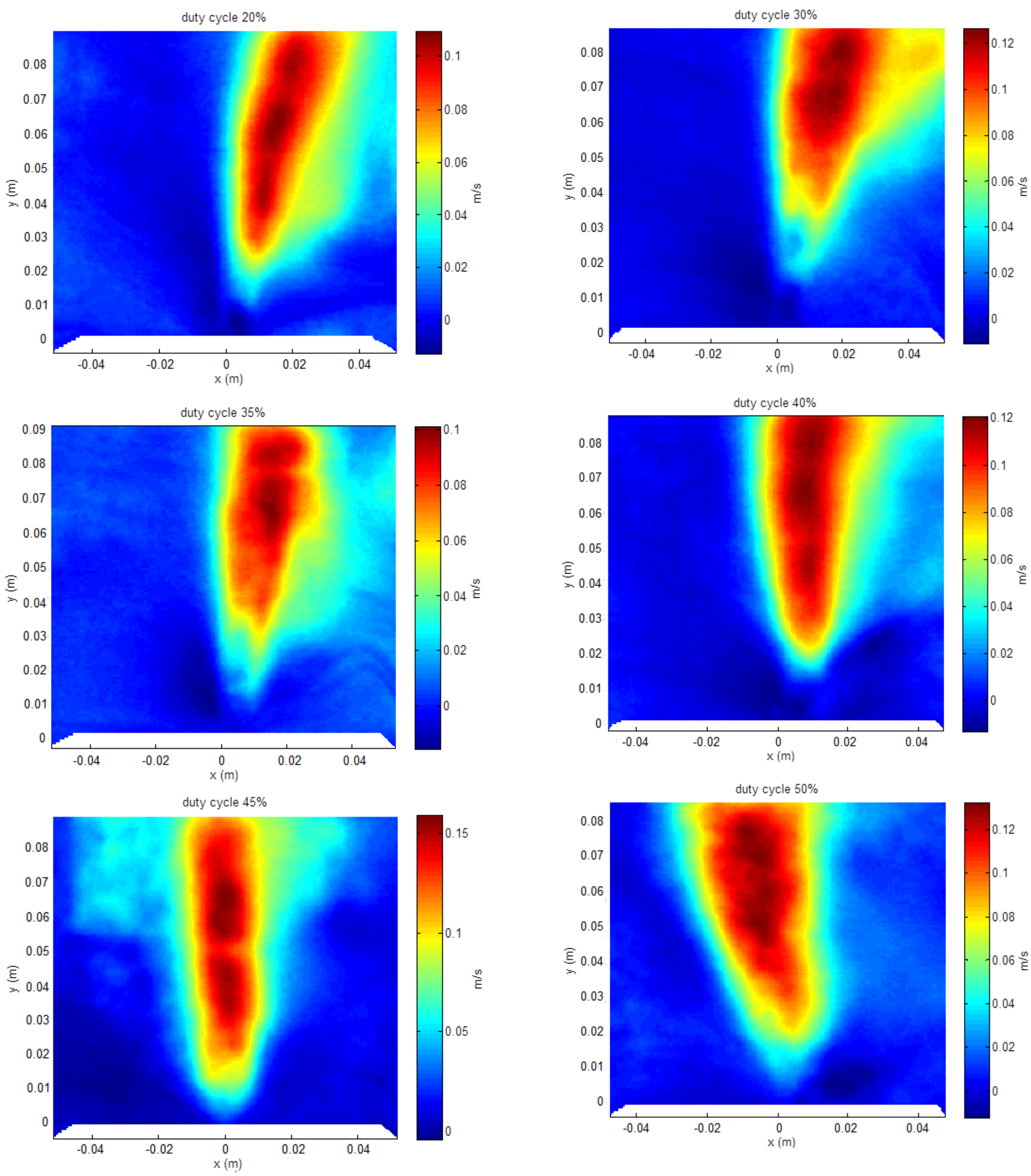

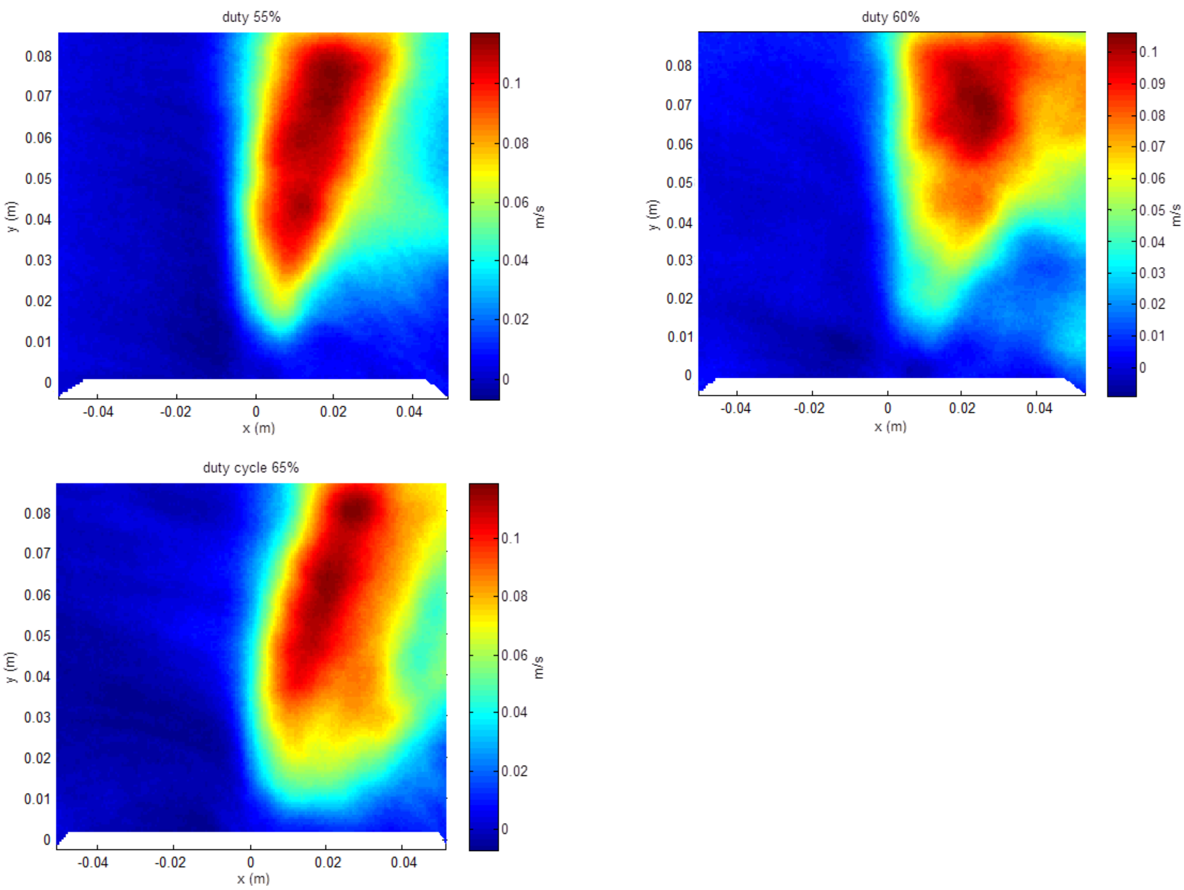
duty 55%
y (m)
x (m)
m/s
duty 60%
y (m)
x (m)
m/s
duty cycle 65%
y (m)
x (m)
m/s

Appendix F

Principles and implementation of the numerical method

The purpose of the model developed by Suzen et al. [37] is to simulate the flow induced by a plasma actuator by solving the Maxwell and Navier-Stokes equations. It models the plasma actuation phenomena by assuming an actuator which has a set voltage applied at the exposed electrode, while at the same time, the embedded electrode is used as a charge density source. The strength of the model lies in decoupling the electric field $\mathbf{E}$ and the charge density ρ_c, both of which are needed to calculate the body force.

The model, however, is phenomenological: it does not give a physical description of the phenomena taking place; it does not in any way model the creation or shape (i.e. microdischarges) of the plasma as such, nor does it take the molecular-scale effects into account that ultimately induce the body force (see the theory in chapter 2).

The type of plasma actuator for which the model was implemented by Suzen et al. is SDBD. In the present study, the same numerical method was used to simulate the flow induced by a PSJA. In this section, the background of the model is explained and a description of the equations, assumptions, and specific parameters and settings used in this study is provided. All computations have been performed using the finite-element software package COMSOL.

F.1 Decoupling E and ρ_c

Gauss' law states that

$$\begin{aligned}\rho_c &= \nabla \cdot \mathbf{D} = \nabla \cdot (\epsilon \mathbf{E}) \\ &= \epsilon_0 \nabla \cdot (\epsilon_r \mathbf{E}),\end{aligned}$$

where ρ_c is the (free) charge density, $\mathbf{D}$ is the electric displacement field, $\mathbf{E}$ is the electric field, ϵ_r is the dielectric constant of the material in question, and ϵ_0 is the standard vacuum permittivity.

Using the relation between electric field and potential $\mathbf{E} = -\nabla\Phi$, Gauss' law can be rewritten to obtain Poisson's equation:

$$\nabla \cdot (\epsilon_r \nabla \Phi) = -\frac{\rho_c}{\epsilon_0}. \tag{F.1}$$

Suzen et al. start from the assumption that the potential in the discharge region can be decomposed into two terms: the externally applied potential, and the potential due to the net charge density in the plasma. The former will be called the the external potential ϕ_{ext} here, the latter will be called the internal potential ϕ_{int}. So,

$$\Phi = \phi_{ext} + \phi_{int}. \tag{F.2}$$

Poisson's equation can now be decomposed as well:

$$\begin{aligned}\nabla \cdot (\epsilon_r \nabla \phi_{ext}) &= -\frac{\rho_{c,ext}}{\epsilon_0} \\ \nabla \cdot (\epsilon_r \nabla \phi_{int}) &= -\frac{\rho_{c,int}}{\epsilon_0}\end{aligned}$$

where $\rho_{c,ext}$ and $\rho_{c,int}$ represent charge densities due to the external and the internal potential, respectively.

Now, the assumption is made by Suzen et al. that the charge density in the air between the electrodes is only due to the internal potential, and remains mostly unaffected by the externally applied voltage, meaning that $\rho_{c,ext} = 0$ and $\rho_{c,int} = \rho_c$ (which is, physically speaking, very unrealistic, because it is the externally applied voltage that induces the discharge in the first place). The decomposed Poisson equation becomes

$$\nabla \cdot (\epsilon_r \nabla \phi_{ext}) = 0$$
$$\nabla \cdot (\epsilon_r \nabla \phi_{int}) = -\frac{\rho_c}{\epsilon_0}. \tag{F.3}$$

The next assumption is that the "internal electric field" $\mathbf{E}_{int} = -\nabla\phi_{int}$ can be neglected relative to the electric field due to the externally applied potential. When this assumption is made, the electric field can be approximated as

$$\mathbf{E} \approx -\nabla \phi_{ext}. \tag{F.4}$$

In this way, ρ_c and $\mathbf{E}$ have been completely decoupled.

F.2 Solving for ρ_c

In order to solve equation F.3, an approach due to Enloe et al. [17] is used to obtain a second relationship between ϕ_{int} and ρ_c, in order to eliminate ϕ_{int} from the equation.

The distribution of the charged particles in the domain depends on their thermal and electrical energy. The corresponding charge density can, according to Enloe et al., be written as:

$$n_{i,e} = n_0 \exp\left[\mp\left(\frac{e\Phi}{k_B T_{i,e}}\right)\right] \approx n_0 \left[1 \mp \left(\frac{e\Phi}{k_B T_{i,e}}\right)\right]$$

where Φ is the local electric potential, $e\Phi$ represents electrical energy, T represents the species' temperature, $k_B T$ represents thermal energy, and n_0 is the background plasma density. The minus sign applies to ions, the plus sign to electrons.

In the Suzen model, as mentioned, it is assumed that the distribution of the charged particles in the plasma is affected solely by the potential caused by that same distribution, i.e. the internal potential. Then, writing ϕ_{int} instead of Φ, the equation becomes

$$n_{i,e} \approx n_0 \left[1 \mp \left(\frac{e\phi_{int}}{k_B T_{i,e}}\right)\right]. \tag{F.5}$$

The net charge density is then represented by:

$$\begin{aligned}
\rho_c &= e(n_i - n_e) \\
&= -en_0 \left(\frac{e\phi_{int}}{k_B T_i} + \frac{e\phi_{int}}{k_B T_e}\right).
\end{aligned}$$

Some rewriting results in

$$\begin{aligned}
-\frac{\rho_c}{\epsilon_0} &= \frac{en_0}{\epsilon_0}\left(\frac{e\phi_{int}}{k_B T_i} + \frac{e\phi_{int}}{k_B T_e}\right) \\
&= \frac{e^2 n_0}{\epsilon_0}\left(\frac{1}{k_B T_i} + \frac{1}{k_B T_e}\right)\phi_{int} \\
&\equiv \frac{1}{\lambda_D^2}\phi_{int}.
\end{aligned}$$

In the last step, λ_D is defined; it is called the Debye length. It follows that the internal potential is given by

$$\phi_{int} = -\frac{\rho_c}{\epsilon_0}\lambda_D^2.$$

Inserting this into equation F.3 results in

$$\nabla \cdot \left(\epsilon_r \nabla \left[-\frac{\rho_c}{\epsilon_0}\lambda_D^2\right]\right) = -\frac{\rho_c}{\epsilon_0},$$

and therefore,

$$\epsilon_r \nabla^2 \rho_c = \frac{\rho_c}{\lambda_D^2}. \tag{F.6}$$

The charge density ρ_c depends on the Debye length λ_D, which in turn depends on the material properties. For air, the Debye length is taken by Suzen et al. to be $1.7\cdot 10^{-4}$ m, while in the dielectric material it is taken to be infinite. In more practical terms, the latter means that plasma will not form in the dielectric.

Equations F.4 and F.6 can now be used independently to compute the electric field $\mathbf{E}$ and charge density ρ_c, respectively.

F.3 Computing the induced velocity field

The body force per unit volume $\mathbf{f}$ is the product of the charge density ρ_c and the electric field $\mathbf{E}$. In a 2D case, it consists of two components:

$$\begin{aligned}
f_x &= \rho_c E_x \\
f_y &= \rho_c E_y
\end{aligned}$$

These terms can be implemented in the Navier-Stokes equation. In the current study, incompressibility is assumed, and the equation is given by

$$\rho\left(\frac{\partial \mathbf{u}}{\partial t} + (\mathbf{u}\cdot\nabla)\mathbf{u}\right) = -\nabla p + \mu\nabla^2\mathbf{u} + \mathbf{f}$$

where $\mathbf{u}$ is the flow velocity vector (ms^{-1}), ρ is the fluid density ($\mathrm{kg{\cdot}m^{-3}}$), μ is the dynamic viscosity of the fluid ($\mathrm{kg{\cdot}m^{-1}s^{-1}}$), p is the pressure (Pa) and $\mathbf{f}$ is the volume force density ($\mathrm{Nm^{-3}}$).

Due to the assumption of incompressibility, the continuity equation reduces to the condition

$$\nabla \cdot \mathbf{u} = 0.$$

In this formulation, the Navier-Stokes equation and the continuity equation can be used to compute the velocity field induced by the volume force.

F.4 Computational domains

The current study uses the above-described model to simulate the flow field induced by L-PSJA operation. For this, a 2D geometry was constructed in COMSOL consisting of 5 domains. A schematic representation (not to scale) of the geometry is given in figure F.1.

The dimensions of the domains and the type of material were chosen such as to most accurately represent the geometry in the actual experiments described in chapters 3-4. The electric field and charge density distribution were solved for in domain 1 and 2. The induced flow field was then computed in domain 1.

F.5 Boundary and initial conditions

In order to solve equations F.4 and F.6, appropriate boundary conditions must be chosen. The procedure for the plasma synthetic jet actuator used here is slightly adapted from the approach detailed by Suzen et al.

The potential at the lower electrode is set to zero. The potential at the upper electrodes is set to a finite value. This value can be constant (representing DC voltage) or time-dependent (representing AC voltage).

Correspondingly, the charge density on the lower electrode is set to some finite value. It must follow the potential at the upper electrodes, i.e. either both are constant, or both are time-dependent in the same way.

The charge density on the upper electrodes is set to zero, as well as the charge density on the bottom surface of the dielectric and the outer boundaries of the air domain.

In a real-life situation, as explained in chapter 2, the potential must be of AC type in order to operate a plasma actuator, due to its self-limiting behavior. In the model, a constant charge density is set on all three electrodes, so the actuator in the model can be "continuously operated" with DC voltage input.

Regarding the Navier-Stokes equation, a no-slip condition is applied on all boundaries of the air domain.

A schematic overview of all boundary conditions used in the present study is given in figure F.2.

The initial condition for the charge density and the potential was set to be zero in domain 1 and 2. The initial velocity of the surrounding air was also set to be zero, meaning that the simulated actuator operated in an initially quiescent environment. The initial pressure was set to 1 atm and ambient temperature was set to 293.15 K.

F.6 Parameters and constants

All other parameters and constants necessary for the computation are given in table F.1. Wherever possible, the values from the real experiments were copied into the model.

F.7 Grid

In the simulations, a "physics controlled mesh", consisting of triangular and quadrilateral shaped elements with a "fine" element size, was used. A picture of the mesh can be seen in figure F.3. The element size was the smallest at the upper electrodes' edges. Close-ups of the mesh can be seen in figures F.4 and F.5. The total number of triangular elements in the mesh was 27490; the number of quadrilateral elements amounted to 1020.

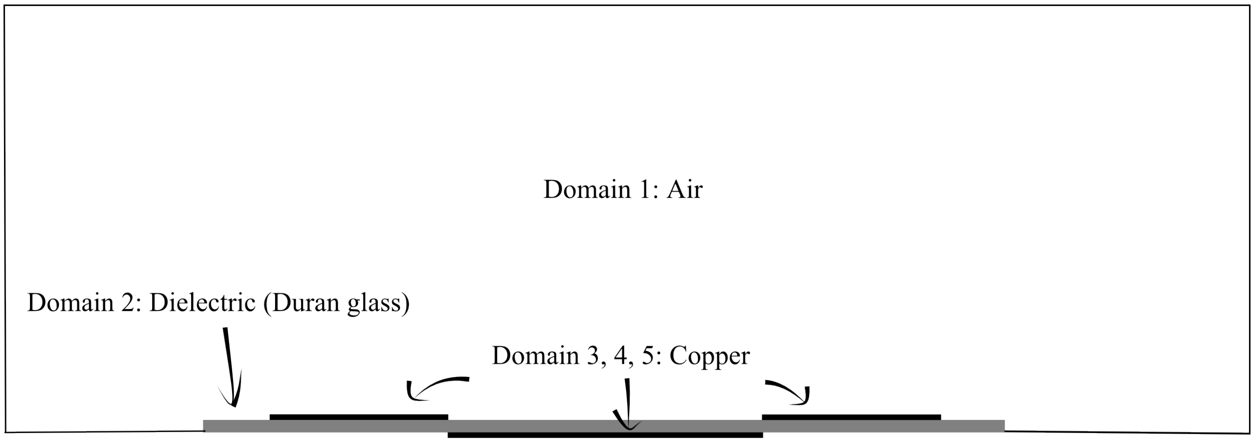

Figure F.1: *Schematic representation of the domains used in the computations*

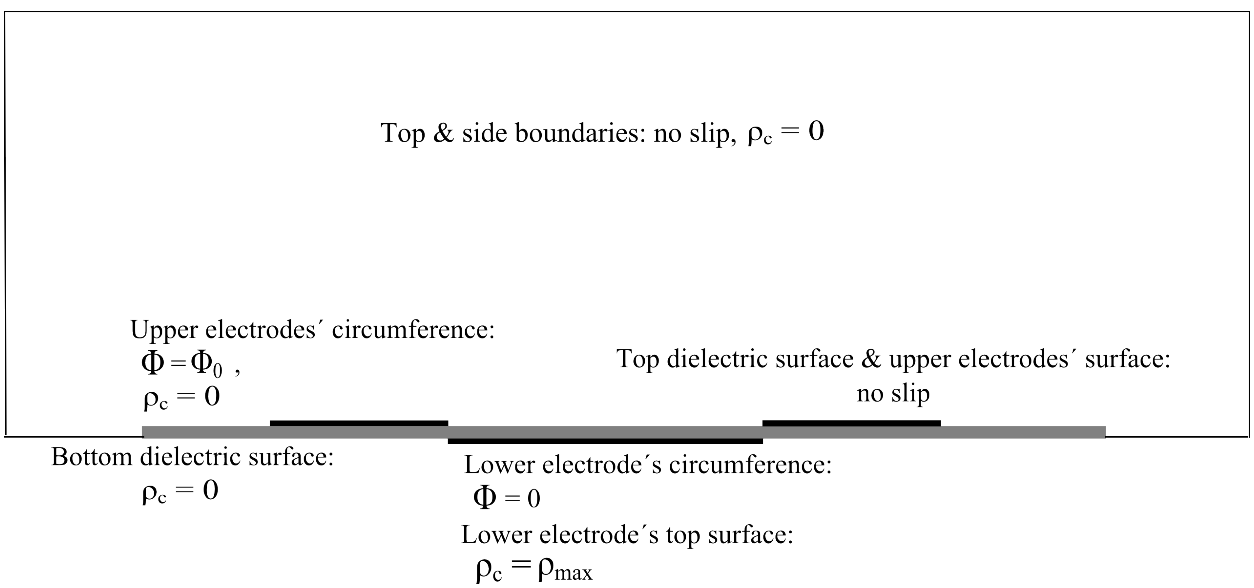

Figure F.2: *Schematic representation of the boundary conditions used in the computations*

Table F.1: *Parameters and constants used in the computations*

Parameter	Value	Origin
Voltage on upper electrodes Φ_0	12 kV	Larger than the experimental amplitudes - this value was used to limit computational time
Debye length in air	$1.7{\cdot}10^{-4}$ m	From Suzen et al. [37]
Debye length in dielectric	∞	From Suzen et al. [37]
Gap between upper & lower electrodes	0 mm	Used in experiments
Width of dielectric	100 mm	Used in experiments
Thickness of dielectric	2 mm	Used in experiments
Lower electrode width	19 mm	Used in experiments
Upper electrode width	10 mm	Used in experiments
Electrode thickness	0.06 mm	Used in experiments
Charge density on lower electrode ρ_{max}	0.0008 Cm^{-3}	From Suzen et al. [37]
Relative electric permittivity of air	1.0	-
Relative electric permittivity of dielectric	4.6	Value for Duran Glass
Size of air domain	0.55 m x 1.19 m	Used in experiments (cabinet)

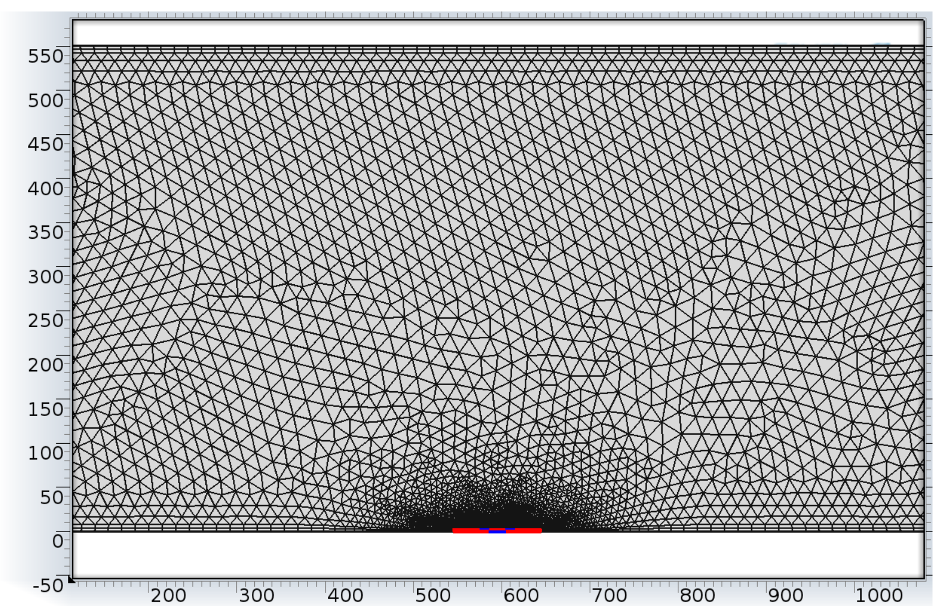

Figure F.3: *The grid used in the computations. Electrodes are displayed in blue, the dielectric in red.*

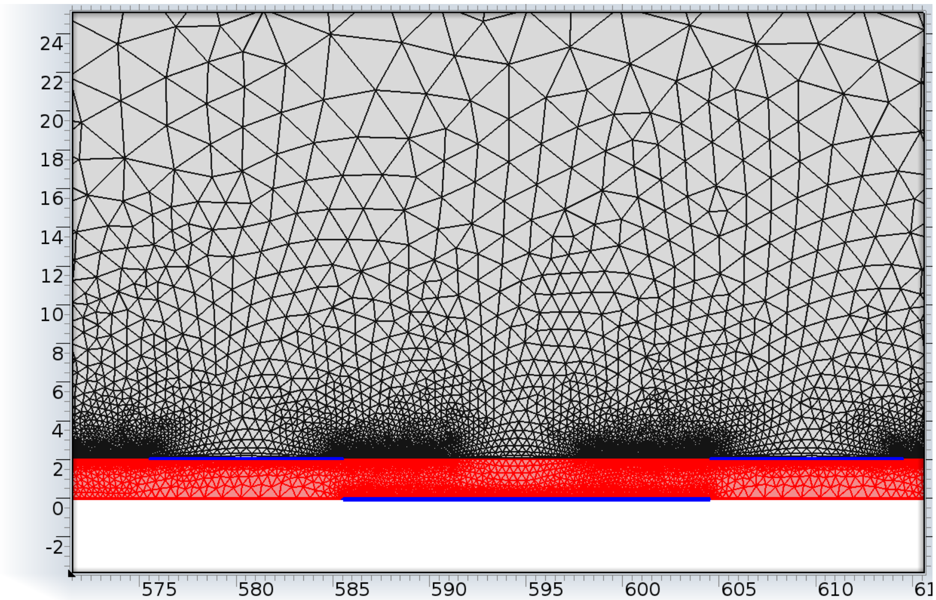

Figure F.4: *Close-up of the grid at the dielectric surface. Electrodes are displayed in blue, the dielectric in red.*

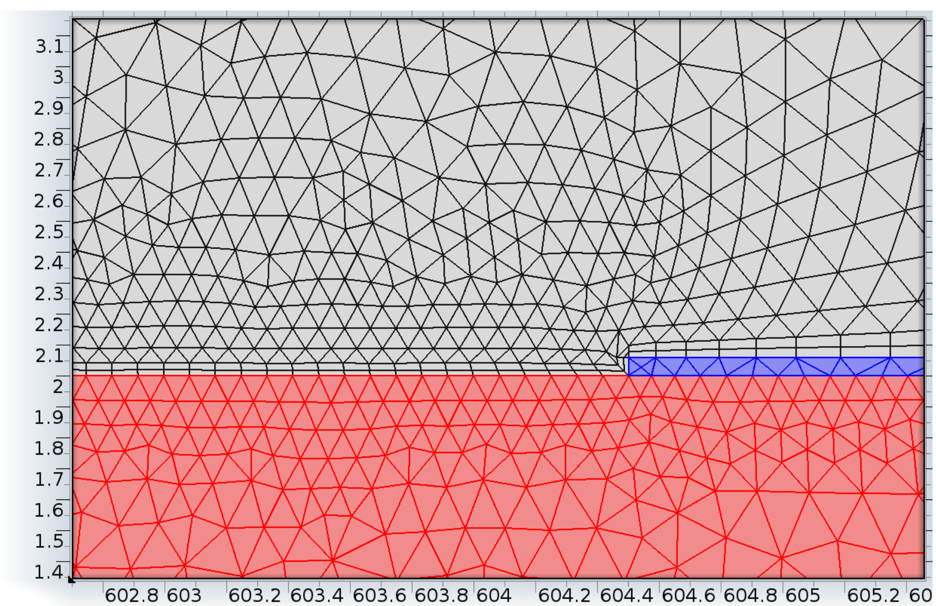

Figure F.5: *Close-up of the grid at an upper electrode's edge. The electrode is displayed in blue, the dielectric in red.*